

# Effects of non-parallelism on standard and magnetorheological measurements

R. Rodrigues<sup>1,3</sup>, F.J. Galindo-Rosales<sup>2,3</sup>, and L. Campo-Deaño<sup>1,3†</sup>

<sup>1</sup>CEFT - Centro de Estudos de Fenómenos de Transporte, Depto. de Engenharia Mecânica, Faculdade de Engenharia, Universidade do Porto, Rua Dr. Roberto Frias, 4200-465, Porto, Portugal

<sup>2</sup>CEFT - Centro de Estudos de Fenómenos de Transporte, Depto. de Engenharia Química, Faculdade de Engenharia, Universidade do Porto, Rua Dr. Roberto Frias, 4200-465, Porto, Portugal

<sup>3</sup>ALiCE - Laboratório Associado em Engenharia Química, Faculdade de Engenharia, Universidade do Porto, Rua Dr. Roberto Frias, 4200-465, Porto, Portugal

<sup>†</sup>Email: [campo@fe.up.pt](mailto:campo@fe.up.pt)

Human blood has a complex composition and unique rheological properties, making it challenging to measure accurately. In addition to this, its mechanical properties may be influenced by external magnetic fields, which, despite being a characteristic of significant interest in the development of new treatment therapies, remains relatively unexplored. To achieve an accurate magnetorheological description of blood, the employed equipment must achieve accurate results taking into account its low viscous and elastic character. However, low and inconsistent apparent-viscosity values were observed systematically in a rotational rheometer equipped with a magnetorheological cell, without the applied magnetic field. In this work, a parametric study was conducted, experimentally and numerically, to evaluate this error source. Steady shear measurements were carried out with low-viscosity Newtonian fluids with two geometries: a parallel-plate, at different gap heights, and a cone-plate. An additional standard bottom plate for non-magnetic testing was also employed for comparison. The standard bottom plate returned constant viscosities near the expected values, whereas the plate attached to the magnetorheological cell showed a clear decrease of measured viscosity with parallel-plate gap reduction and an increase in cone-plate-measured viscosity. Numerical results corroborated the experimental observations, pointing towards an inclination of the bottom magnetic plate which can significantly affect the flow. Additional experimental and numerical work was conducted to evaluate the effects of the setup imperfection on magnetorheological measurements, unveiling magnetorheology's deep dependence on the geometric characteristics.

**Keywords:** Rotational rheometry; Steady shear; Gap-error; Magnetorheology; low-viscous fluids

# 1 Introduction

Blood is a complex fluid because of its composition and mechanical properties. It is essentially a suspension of blood cells in plasma. Blood cells can be characterised as thrombocytes (or platelets), leukocytes (white blood cells or WBCs) and erythrocytes (red blood cells or RBCs), the latter being the most predominant in blood, with volume concentration, or haematocrit (Htc), between 40 to 54% in men and 36 to 48% in women, depending on other factors such as diseased state, altitude, etc.<sup>1</sup> Blood rheology highly depends on plasma viscoelasticity, haematocrit and RBCs' mechanical properties and aggregation mechanisms. In terms of viscous response, blood is a shear-thinning fluid with a relatively low high-shear viscosity<sup>2</sup> (around 3 mPa·s). Moreover, RBCs are composed of haemoglobin, which incorporates iron. When not carrying oxygen (deoxyhaemoglobin), free electrons make it paramagnetic (attracted to an external magnetic field), while carrying oxygen (oxyhaemoglobin), it remains diamagnetic (slightly repulsed)<sup>3</sup>. This makes RBCs and, as a consequence, whole blood susceptible to magnetic fields. In recent years, the efforts of the scientific community to understand the effects of magnetic fields on blood's rheological properties have grown. Magnetic fields have been studied as means of guidance for microrobots and particles for a multitude of medical applications<sup>4–7</sup> and also to knowingly alter blood's properties themselves<sup>8</sup>, making magnetohaemorheology a field of significant interest. However, experimental data are still lacking, and a full magnetorheological description of whole blood has yet to be achieved.

Measurements with low-viscosity fluids, such as blood, can be strenuous even when considering simple fluids. Rotational rheometers, equipped with a magnetorheological cell to generate a uniform magnetic field, are commonly used to perform magnetorheological characterisations of this kind of fluids. Therefore, addressing some common error sources in rotational rheometry that could negatively affect the results is essential. A more in-depth walkthrough of such experimental difficulties is given in the seminal work of [Ewoldt et al.](#). Relevant to this work, we shall focus on the flow of low-viscosity Newtonian fluids and suspensions under steady shear in planar geometries (parallel-plates, PP, and cone-plate, CP).

The steady shear viscosity,  $\eta$ , can be obtained through the shear stress,  $\sigma$ , and the shear rate<sup>i</sup>,  $\dot{\gamma}$ , as given in the following equation<sup>9</sup>:

$$\eta = \frac{\sigma}{\dot{\gamma}} = \frac{F_{\tau}T}{F_{\gamma}\Omega}, \quad (1)$$

where  $T$  is the torque,  $\Omega$  is the rotational velocity and  $F_{\tau}$  and  $F_{\gamma}$  are functions of geometrical characteristics, which for PP and CP geometries are given by<sup>9</sup>:

$$\text{PP : } \quad F_{\tau} = \frac{2}{\pi R^3} \quad \text{and} \quad F_{\gamma} = \frac{R}{h}, \quad (2)$$

$$\text{CP : } \quad F_{\tau} = \frac{3}{2\pi R^3} \quad \text{and} \quad F_{\gamma} = \frac{1}{\beta}, \quad (3)$$

---

<sup>i</sup>Either can be the controlled input, depending on the instrument.

where  $R$  is the geometry radius,  $h$  is the gap between parallel-plates and  $\beta$  is the CP cone angle.

Steady shear measurements are limited by the minimum and maximum torques of the rheometer,  $T_{\min}$  and  $T_{\max}$ , and the maximum angular velocity is  $\Omega_{\max}$ . Given that the viscosity results are usually plotted as a function of the shear rate, the valid range in the  $\eta(\dot{\gamma})$  space is limited by the following expressions:

$$\frac{F_{\tau} T_{\min}}{\dot{\gamma}} < \eta < \frac{F_{\tau} T_{\max}}{\dot{\gamma}}, \quad (4)$$

$$\dot{\gamma} < F_{\gamma} \Omega_{\max}. \quad (5)$$

To obtain viscosity curves, it is common to collect viscosity data at several shear rates in a single test, which implies a shear rate step between data points. This requires some attention to obtain quality data, first due to the non-infinite acceleration of the rheometer and, second, because the flow does not instantly regain a steady state. Thus, a constant time interval is usually defined for the rheometer to wait between the shear rate step and the measurement. Another approach is to define a time function that establishes this waiting period, dependent on the shear rate, whether linear, exponential, logarithmic, or other. This latter method is helpful because, usually, the flow stabilises faster for larger rotational velocities; thus, having the time step diminish with the shear rate may reduce the overall measurement time. In any case, it is usual to perform preliminary constant-shear-rate measurements (at different shear rates) to evaluate the required time intervals. If this is not considered, one may be gathering unsteady flow data.

Centrifugal forces at sufficiently high rotational velocities lead to an outward radial velocity component at the moving boundary and, at the static plate, from mass conservation, an inward radial component, i.e., secondary flows. This phenomenon leads to an increase in measured torque and is responsible for an apparent shear-thickening at high shear rates. From an analysis of experimental data, [Turian](#) arrived at an expression which allows us to estimate the experimental region free from secondary flows. By adjusting their expression, we can obtain another experimental limit:

$$\eta < \frac{\rho \dot{\gamma} R^2}{4F_{\gamma}^3}. \quad (6)$$

Increasing the rotational velocity further, the sample may escape the geometry, leading to decreased sample volume and an abrupt drop in measured viscosity.

Considering the loading conditions of the sample, over- and underfilling can lead to significant errors. Overfilling the geometry may lead to additional torque depending on the amount of extra sample volume and geometrical characteristics<sup>11</sup>. On the other hand, underfilling will result in a lower apparent viscosity because the sample cannot completely fill the geometry. Additionally, the symmetry of the sample/air interface is paramount for low shear measurements. [Johnston and Ewoldt](#) concluded from mathematical analysis that an additional torque can arise from non-constant surface tension, or non-constant contact angle, between the fluid sample and the plates. Essentially, asymmetries in the contact line lead to surface tension forces that pull along the fluid/air interface,

resulting in an additional torque, which is more significant at low shear, thus leading to an apparent shear-thinning behaviour that vanishes at sufficiently high shear rates. Sample evaporation and over/underfilling are also sources of surface tension torque<sup>12</sup>. This issue can be mitigated by accurate sample volume, reducing sample evaporation and diminishing the fluid's surface tension<sup>12</sup>. Moreover, placing the sample perfectly at the centre of the geometry aids in reducing contact line asymmetry as far as the wetting conditions of the plates allow. Despite all the efforts to counteract this phenomenon, it can still lead to torque artefacts up to two orders of magnitude larger than the rheometer's minimum torque. Thus, it has been common practice to multiply the low-torque limit by a safety coefficient, shifting it to a higher shear.

Geometrical characteristics can also affect measurement quality. Deviations from the nominal dimensions and unwanted rougher surface finishing from fabrication errors or wear can result in incorrectly measured viscosities. Apart from the geometries' characteristics, errors in the gap height between the plates (or the cone and plate) can also lead to significant errors. Gap-errors can arise from a multitude of factors<sup>13</sup>. Setting zero-gap is usually done by lowering the moving plate until an increase in normal force is sensed, signalling solid-solid contact. However, if the threshold force for contact assumption is not sufficiently high ( $\lesssim 5$  N), normal forces arising from air squeeze can incorrectly serve as the contact input, leading to a deviation of the zero-gap by a few micrometers<sup>14</sup>. Deviations in the surface finishing of either plate and non-parallelism of the geometry may also lead to gap errors. In any case, the usual gap-error leads to the actual/average gap in the geometry being more significant than the commanded gap in the rheometer interface around 10 to 50  $\mu\text{m}$ <sup>9</sup>, which leads to experimental issues. Not accounting the gap-error can result in sample underfilling if the correct geometry loading is not, or cannot be verified before initiating the measurements. Moreover, even with perfect loading, gap-errors must not be disregarded, particularly for small gaps. Having that the error is constant for a set of experiments, it results in lower apparent viscosities for smaller gaps, whereas, for progressively larger gaps, the results approach the fluid's actual viscosity due to the decreased relevance of the gap-error. Now, considering a PP system (for CP geometries, the gap is fixed by default), having the real gap as the sum of the commanded gap and a gap-error:  $h_r = h_c + \epsilon$ , a divergence between the commanded and applied shear rates arises:  $\dot{\gamma}_c = (R/h_c)\Omega$ ,  $\dot{\gamma}_r = (R/(h_c + \epsilon))\Omega$ . With some manipulation, we can obtain:

$$\frac{h_c}{\eta_m} = \left(\frac{1}{\eta_r}\right) h_c + \frac{\epsilon}{\eta_r}, \quad (7)$$

where  $\eta_m$  and  $\eta_r$  are the measured and real viscosities, respectively. This expression is a variation of the one given by Kramer et al. and allows for an estimation of the fluid's true viscosity,  $\eta_r$ , and the gap-error,  $\epsilon$ , by conducting measurements at multiple gap heights. It is, however, noteworthy that through this analysis slip effects cannot be decoupled from a gap-error as these return a similar measured-viscosity decrease with gap height reduction<sup>16</sup>.

Regarding suspensions, several phenomena must be taken into account. Here we focus on dilute/semi-dilute suspensions of spherical particles (volume fractions below 0.25). Brownian motion, inertial effects and the overall ability of the particles to follow the



fluid flow are important and should be evaluated. The Peclet ( $Pe$ ), (particle) Reynolds ( $Re_p$ ) and Stokes ( $St$ ) numbers are used to quantify these respective effects which may be generally disregarded if the following adimensional quantities are sufficiently small<sup>17</sup>:

$$\frac{1}{Pe} = \frac{k_B T}{6 \pi \eta (d_p/2)^3 \dot{\gamma}}, \quad (8)$$

$$Re_p = \frac{\rho (d_p/2)^2 \dot{\gamma}}{\eta}, \quad (9)$$

$$St = \frac{\rho_p d_p^2 \dot{\gamma}}{18 \eta}. \quad (10)$$

$d_p$  and  $\rho_p$  are the particle diameter and density, respectively,  $k_B$  is the Boltzmann constant and  $T$  is the temperature. Additionally, gravitational effects can be relevant if the density difference between the dispersed and continuous phases is significant, and particle migration may occur either from shear rate gradients within the flow or particle surface roughness and collisions<sup>17</sup>. This particle movement may lead to the formation concentration gradients, originating depletion layers near the solid boundaries or even shear banding. Particle depletion near the geometry walls provokes an apparent slip of the dispersed phase and is common in suspension rheology, resulting in a viscosity gap-dependence and may be corrected a posteriori or counteracted by increasing the surface roughness or detailing the geometry (milled or serrated, for example)<sup>18,19</sup>. Suspensions may also display time-dependent behaviour as the microstructure takes time to adjust to the applied shear. Moreover, the rheological response is also dependent on the shear history, particularly for small shear rates or after a resting period where the suspension may achieve a metastable state<sup>17</sup>.

Concerning magnetorheological measurements, the application of an external magnetic field induces magnetic dipoles in the individual particles, causing them to aggregate into elongated chains aligned with the magnetic field lines<sup>17</sup>. As such, a reversible and controllable microstructure is enabled that can significantly alter the bulk rheological properties<sup>20</sup>. Additional experimental concerns arise from the time-dependent nature of the structure formation/destruction mechanisms and heating from magnetic field generation, which can be significant for strong fields.

All these experimental limitations and phenomena can compromise measurement quality and, because whole blood is a precious fluid, it is vital to identify the possible error sources and define an experimental window before tackling its magnetorheological characterisation. In this work, steady shear measurements were performed with different Newtonian fluids in two static bottom plates and two planar geometries (PP and CP), and the experimental limits were defined and discussed. Measurements were also conducted with a Newtonian fluid seeded with magnetic particles in different concentrations under an external magnetic field of varying intensity. Numerical simulations were conducted to evaluate the effects of a possible error source on standard and magnetorheological measurements.

## 2 Materials and methods

### 2.1 Rheometer and accessories

An Anton Paar MCR302-e stress-controlled rotational rheometer, shown in Figure 1(a), was used for the rheological characterisation. According to the supplier, the instrument's limitations were:  $T_{\min} = 1 \text{ nN}\cdot\text{m}$ ,  $T_{\max} = 230 \text{ mN}\cdot\text{m}$  and  $\Omega_{\max} = 314 \text{ rad/s}$ .

Two static bottom plates were used; one was designed explicitly for magnetorheological measurements (Magnetic Plate, or MP) and the other for standard testing (Standard Plate or SP), both are shown in Figure 1(b). The SP had a diameter of 50 mm and allowed for careful temperature control through a Peltier system. On the other hand, the MP had a diameter of about 30 mm and was attached to a magnetorheological cell, which fit into the rheometer and was connected to a power source (being responsible for the generation of the magnetic field) and to an external cooling system filled with water, which allowed to dissipate heat from the magnetic field generation, but keeping a precise temperature control within the fluid sample still remained challenging. The MP itself was fixed to the cell by two screws and centred by three radial fixtures, as can be seen in Figure 1(b2).

Two upper geometries were considered, one parallel-plate (PP20 MRD) and one truncated cone-plate (CP20 MRD), specially designed for magnetorheological measurements. Both had a diameter of 20 mm, and the CP had a cone angle of  $1.981^\circ$  and a truncation height of 0.084 mm. Both geometries can be seen in Figure 1(c). Either MRD geometry has an outer region consisting of two rings with different depths (both lesser than the plate itself) that hinder the visualisation of the loading quality. In the SP, we could still visualise the sample's profile with a high-contrast background (white walls in our case). On the other hand, the MP also had an outer rim, which completely blocked our vision of the contact line in the MRD geometries, making evaluating the loading quality impossible. Figure 2 shows a schematic of the PP20 MRD with either bottom plate.

The magnetorheological cell was able to generate a magnetic field perpendicular to the flow direction, measured with an FH 54 teslameter (MAGNET-PHYSIK) inserted into a slot underneath (depicted in Figure 2). The geometries (PP20 MRD and CP20 MRD) were non-magnetic, which prevented radial forces from acting on the shafts, and the magnetic circuit was closed with a yoke placed on top of the geometry<sup>21</sup>. In this study, a working fluid was seeded with M-270 Carboxylic Acid Dynabeads™ (Thermo Fisher Scientific) paramagnetic particles with  $2.8 \text{ }\mu\text{m}$  diameter, density of  $1600 \text{ kg/m}^3$  and their magnetisation curve is given by Grob et al. (saturation of  $6.4 \text{ Am}^2/\text{kg}$  for  $B \gtrsim 500 \text{ mT}$ ).

### 2.2 Working fluids

Four different Newtonian fluids were used: a calibration oil provided by Anton Paar (Cal. Oil), two aqueous solutions of glycerol in mass concentrations of 75.20 and 93.05 wt% (75.20Gly and 93.05Gly, respectively), and an aqueous solution of 52 wt% of Dimethyl sulfoxide (DMSO) (Newtonian blood analogue<sup>23</sup>, NBa). Table 1 gives each working fluid's compositions, expected densities, and viscosities at the experimental temperature of  $20^\circ\text{C}$ .

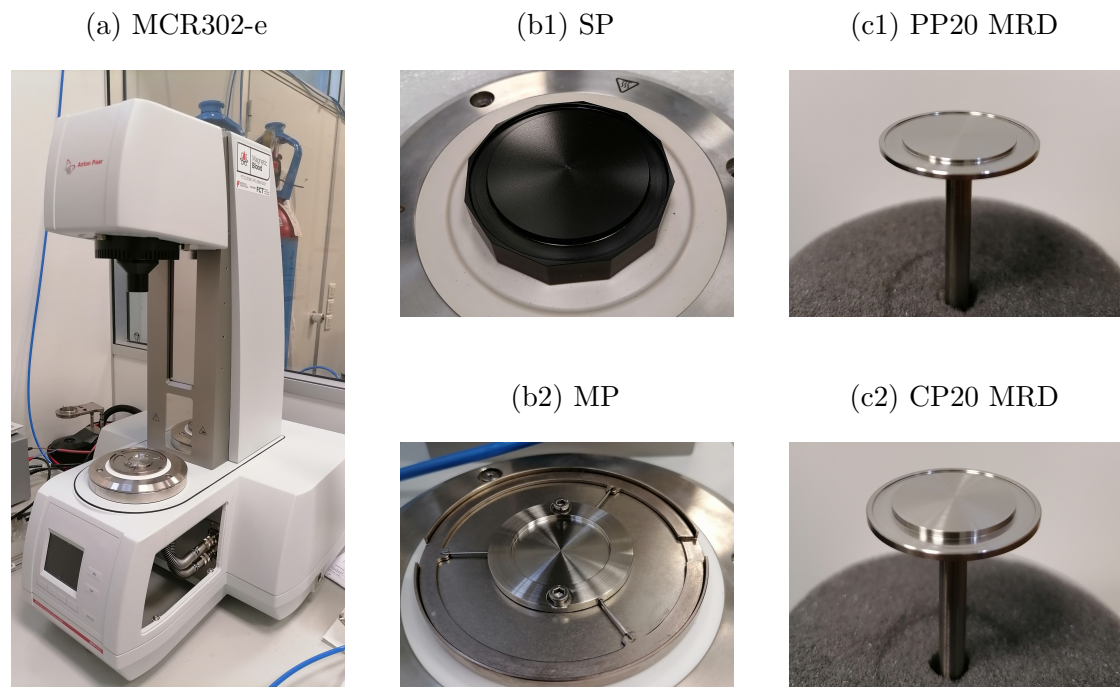


Figure 1: Experimental setup: (a) Anton Paar MCR302-e rotational rheometer, (b) SP and MP bottom plates, and (c) PP20 MRD and CP20 MRD geometries.

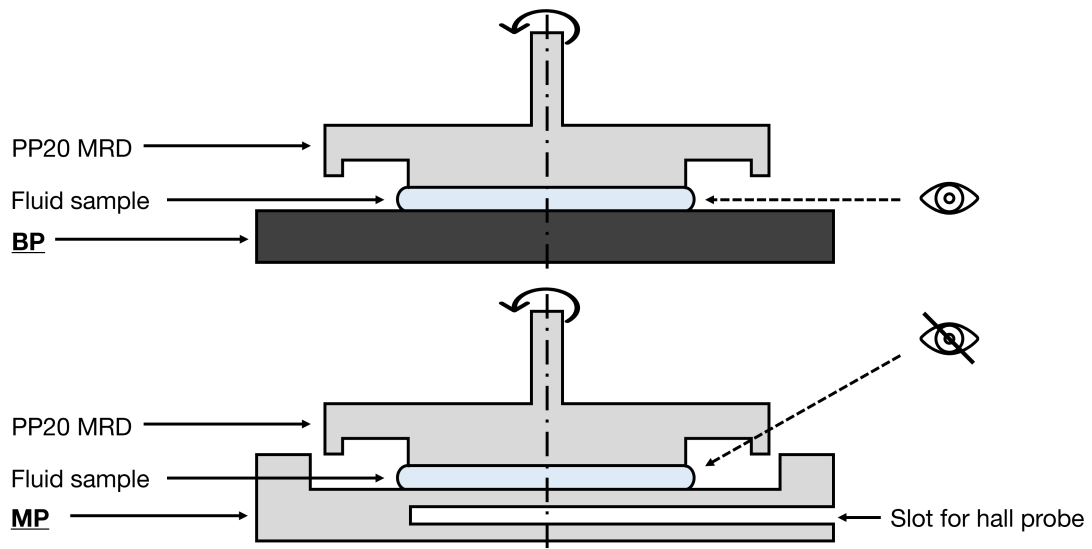


Figure 2: Schematic of the PP20 MRD geometry on either bottom plate (not to scale) and associated difficulties with evaluating the loading quality.

Table 1: Composition and expected viscosity,  $\eta$ , and density,  $\rho$ , of the working fluids (at 20°C). Calibration oil data from the supplier (Anton Paar). Glycerol and water estimates from Volk and Kähler. DMSO data from Budeanu and Dumitrescu

Sample	Water [wt%]	Glycerol [wt%]	Cal. Oil [wt%]	DMSO [wt%]	$\rho$ [kg/m <sup>3</sup> ]	$\eta$ [mPa·s]
Cal. Oil	-	-	100	-	816.1	3.66
75.20Gly	24.80	75.20	-	-	1194.9	36.98
93.05Gly	6.95	93.05	-	-	1243.0	365.68
NBa	48.00	-	-	52.00	1051	3.32

## 2.3 Experimental procedure

Before any measurement, the zero-gap was set, the inertia of both the drive and the measuring system was acquired, and a motor adjustment function was conducted according to the RheoCompass™ (Anton Paar) procedure. The set zero-gap and inertia call operations were repeated at every rheometer reset and bottom plate/geometry switch. Also, both plates were thoroughly cleaned of any previous sample residues and dust particles, cleansed with ethanol and dried with compressed air. The sample volume (previously determined and given as supplementary material) was accurately measured with a VWR® standard line precision pipette and carefully applied at the centre of the bottom plate. Measurements with the calibration oil required the fluid sample to be applied on the top plate/cone instead, or a combination of both, due to the fluid’s low surface tension. The rheometer head was then lowered with the predefined viscoelastic movement profile. When possible, the loading quality was evaluated before measurement started, looking for any signs of under/overfilling and contact line asymmetry.

The viscosity was measured by imposing a shear rate logarithmic ramp-up with about 10 points per decade, between  $10^{-1}$  and  $10^4$  s<sup>-1</sup>. A constant waiting time of a few seconds was defined between shear rate shift and data acquisition, guaranteeing steady flow. For all measurements, at least 5 tests were conducted for statistical robustness, posteriorly averaged, and the 95% confidence intervals calculated using Student’s t-distribution.

With the SP, the Peltier system was set to maintain a constant temperature (20°C), whereas no such fine temperature control was achievable with the MP. Our approach was to conduct the measurements when the room temperature did not diverge too much from the analogous tests with the SP (maximum  $\pm 5^\circ\text{C}$ ) while keeping the average temperature of the measurement set close to the targeted 20°C.

Concerning the magnetorheological measurements, prior to loading, the samples were thoroughly mixed to redisperse the sedimented particles and to break any possible microstructure that may have formed at rest. The steady shear viscosity data was gathered at a constant shear rate and 10 magnetic field density values were applied up to  $B \leq 720$  mT. The time interval between field density change and data acquisition was set to 20 s to guaranty a steady state, avoiding gathering data before the magnetic-induced

microstructure was formed.

### 3 Results and discussion

Preliminary experimental results pointed towards a non-negligible gap-error of the MP. Larger sample volumes are required to fill geometries on the MP than on the SP, and a viscosity dependence on the gap height was found, with lower measured viscosities for smaller gaps. The discussion on these preliminary measurements is presented as supplementary material.

#### 3.1 Standard measurements

We set out to test the measurement quality with three Newtonian fluids of different viscosities (Cal. Oil, 75.20Gly and 93.05Gly) on both geometries (PP20 MRD and CP MRD) and both bottom plates (SP and MP). The PP20 MRD gap height was varied between 0.05 and 0.35 mm and Figure 3 shows the obtained viscosity curves. The measured viscosity was plotted along with the experimental limits associated with the rheometer's specifications: torque,  $T_{\max/\min}$ , and rotational velocity,  $\Omega_{\max}$ , and the prediction of secondary flow onset (expressions 4-6); if any are not visible it is because they fall out of the experimental window and are, thus, not relevant for those particular measurements.

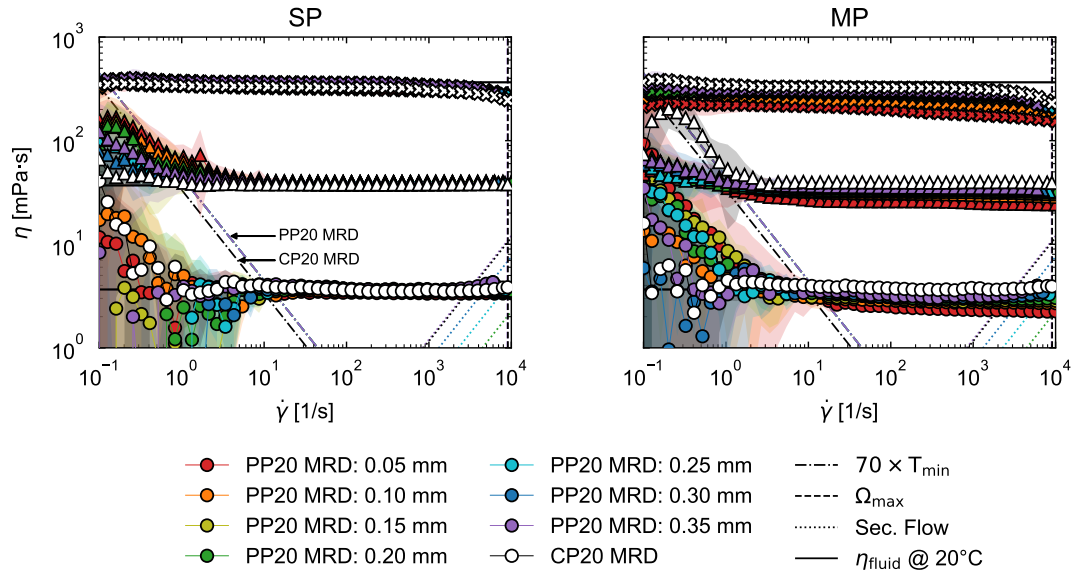


Figure 3: Viscosity curves obtained with three Newtonian fluids: Cal. Oil (circular markers), 75.20Gly (triangular markers) and 93.05Gly (cross markers), on either bottom plate: (left) SP and (right) MP. Data gathered with the CP20 MRD and PP20 MRD (gap heights between 0.05 and 0.35 mm).

The results obtained with the SP show generally constant viscosities for all three tested fluids, with no significant differences between either geometry or PP gap heights. Large errors can be seen at low shear with the two lower viscosity fluids, which should be associated with low-torque issues. Because the rheometer’s minimum torque limit is outside the experimental window (at lower shear rates for the shown viscosity range), we believe these low-shear errors are probably due to surface tension torque from contact line asymmetry<sup>12</sup>. Applying an adjustment factor of 70 to the minimum-torque limit ( $70 \times T_{\min}$ ) seems to predict the low-shear errors accurately but significantly limits the experimental window. Despite our effort to carefully evaluate the correct sample volume, the design of the MRD geometries makes it a strenuous task, not allowing for a visualisation of the contact line throughout the measurement, which may have allowed small loading errors to remain unnoticed. The adjusted torque  $70 \times T_{\min} = 70 \text{ nN}\cdot\text{m}$  however, is, despite significant, not shocking. Johnston and Ewoldt report measured torques with water up to  $1 \text{ }\mu\text{N}\cdot\text{m}$  at low shear from loading errors. Other works, despite employing lesser adjustment factors also had less torque resolution at low shear<sup>26–28</sup>.

At high shear, a slight viscosity increase can be observed for the less viscous fluid on the larger PP gaps and the CP, which is related to secondary flow onset and is accurately predicted by the respective limit<sup>10</sup>. The most viscous solution shows evidence of viscous heating, visible through an acute viscosity decrease at high shear (there was no evidence of sample loss). Even though the SP can guarantee a near-constant temperature via the Peltier system, the temperature sensor is not in direct contact with the fluid sample. Thus, delays in temperature control are not surprising when dealing with very sharp temperature variations in the sample. Additionally, with the 93.05Gly solution a slight viscosity decrease is noted throughout the whole viscosity curve. At low to medium shear this should not be a symptom of viscous heating, as the imposed rotational velocity is relatively low, but it might be due to water absorption over time, which may be more noticeable for small gaps<sup>29</sup>. The same effect may not be as noticeable for the 75.20Gly due to its lesser glycerol concentration.

With the MP, the adjusted low-torque and secondary flow limits also predict the low-shear errors and high-shear measured viscosity increment and the viscous heating effects on the most viscous solution are not significantly more pronounced with the MP. Compared to the SP data, on the MP, the CP20 MRD returned slightly larger viscosities, while with the PP20 MRD, there is a clear viscosity reduction with a gap decrease.

Focusing on the PP20 MRD results, we can conduct a more in-depth analysis by evaluating useful data at multiple gap-heights. To avoid experimental errors, the data selected from each fluid was limited to a particular shear rate range that avoided low-shear uncertainties and secondary flow/viscous heating issues at high shear:  $20 \leq \dot{\gamma}_{\text{Cal.Oil}} \leq 2000$ ,  $3 \leq \dot{\gamma}_{75.20\text{Gly}} \leq 6000$  and  $0.2 \leq \dot{\gamma}_{93.05\text{Gly}} \leq 3000 \text{ s}^{-1}$ . The data obtained at each gap height was averaged over the selected shear rate range,  $\overline{\eta_m}$ , and compared to the expected value,  $\eta_{\text{exp}}$ . (Table 1), through a relative error:

$$\text{R.E.} = \frac{\overline{\eta_m} - \eta_{\text{exp.}}}{\eta_{\text{exp.}}}, \quad (11)$$

which is shown, for each fluid, in Figure 4.



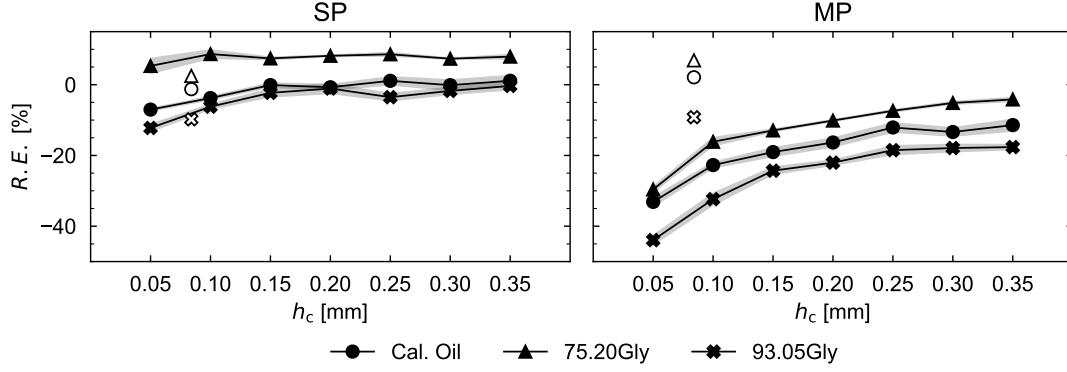


Figure 4: Mean viscosity relative errors and respective 95% confidence intervals for all three fluids: Cal. Oil (circular markers), 75.20Gly (triangular markers) and 93.05Gly (cross markers), gathered on both geometries: PP20 MRD (filled markers) and CP20 MRD (empty markers), and on either bottom plate: (left) SP and (right) MP. Confidence intervals for the CP20 MRD always within marker size.

The measured viscosity dependence with PP gap height is evident with the MP. With this bottom plate, for the lowest PP gap of 0.05 mm, the relative error is significant, between -45 and -30%, but it diminishes with increasing gap height to errors between -18 and -4% for  $h_c = 0.35$  mm. With the CP20 MRD, however, positive relative errors are noticed for the two least viscous fluids (2 and 7%), while the most viscous solution (93.05Gly) returned a negative error of -9%. It is important to remember that with the 93.05Gly solution, we did notice a viscosity decrease along the curve, possibly due to water absorption, which may be why this fluid shows more significant relative errors. Although the SP's relative errors are not as striking as the MP's, we can still notice a slight dependence of the measured viscosity with gap height. The Cal. Oil and 93.05Gly tend to a null relative error with gap increase, while the 75.20Gly solution presents a weak tendency towards a 7% positive error which could be due to an inaccurate preparation of the solution, where the glycerol concentration was slightly larger than intended. The CP20 MRD returned lesser errors than on the MP, with the two less viscous fluids approaching a null error.

Because this viscosity gap-dependence is not observed on the SP, we believe there is a systematic gap-error on the MP and that slip effects are negligible. As such, fitting this gap-varying data to Equation 7, we can estimate the gap-error,  $\varepsilon$ , and correct the measured viscosity to an estimated value<sup>15</sup>:  $\eta_r = \bar{\eta}_m (1 + \varepsilon/h_c)$ . The fitting procedure was done using Python's Statsmodels GLM functionalities, and Figure 5 shows the estimated gap-errors and corrected viscosities for each fluid.

On the SP, the 75.20Gly solution returned a practically null gap-error, while small values are observed for the Cal. Oil and the 93.05Gly. These non-zero estimated gap-errors may have arisen from measurement uncertainty with the low-viscosity Cal. Oil, whereas for the high-concentration glycerol solution it may be a result of the previously-mentioned water absorption. From these results we assume hereafter that there is no gap-error on



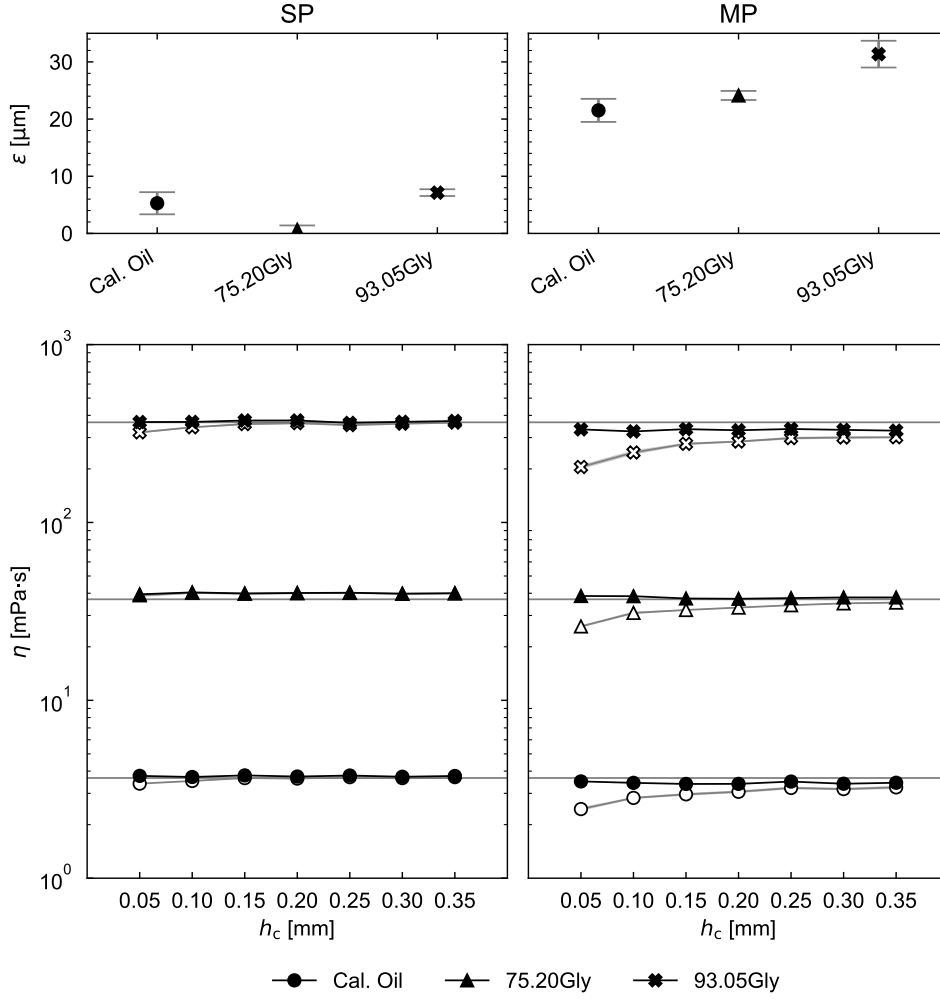


Figure 5: Gap-error,  $\varepsilon$ , and true viscosity estimates,  $\eta_r$  (filled markers, with averaged measured viscosity,  $\bar{\eta}_m$ , in open markers for comparison) for all three fluids: Cal. Oil (circular markers), 75.20Gly (triangular markers) and 93.05Gly (cross markers), on either bottom plate: (left) SP and (right) MP.

the SP. Contrarily, on the MP the Cal. Oil and 75.20Gly point towards a gap error of approximately 22.8  $\mu\text{m}$ , while the 93.05Gly solution again presents a larger estimation. The corrections on the MP returned slightly lesser viscosities than on the SP, which could be due to deviations of the mean room temperature from 20°C during measurement (the recorded mean temperatures were 21.1, 20.3 and 20.8°C, for the Cal. Oil, 75.20Gly and 93.05Gly), but overall the actual viscosity estimates do seem to effectively predict the fluids' true viscosities.

Once an efficient method to estimate the fluids' actual viscosities is validated, we can correct the experimental viscosity curves through two approaches. The first consists of correcting the viscosity by performing gap-error and true viscosity estimates at all shear rates which could return some statistically interesting data, but this method would also be accounting for errors associated with the experimental limits when considering viscosity data obtained at extreme shear rates (either too low, from the rheometer's minimum torque or surface tension torque from contact line asymmetry, or too high, from secondary flow onset and viscous heating). The alternative is to employ the previously obtained MP gap-error ( $\varepsilon_{\text{MP}} \approx 22.8 \mu\text{m}$ ) to correct the measured viscosity at all shear rates ( $\eta_m (1 + \varepsilon/h_c)$ ). As the gap-error was estimated through viscosity data within the experimental window, we opted for this second method and Figure 6 shows the corrected viscosity curves (the SP data remained unaltered).

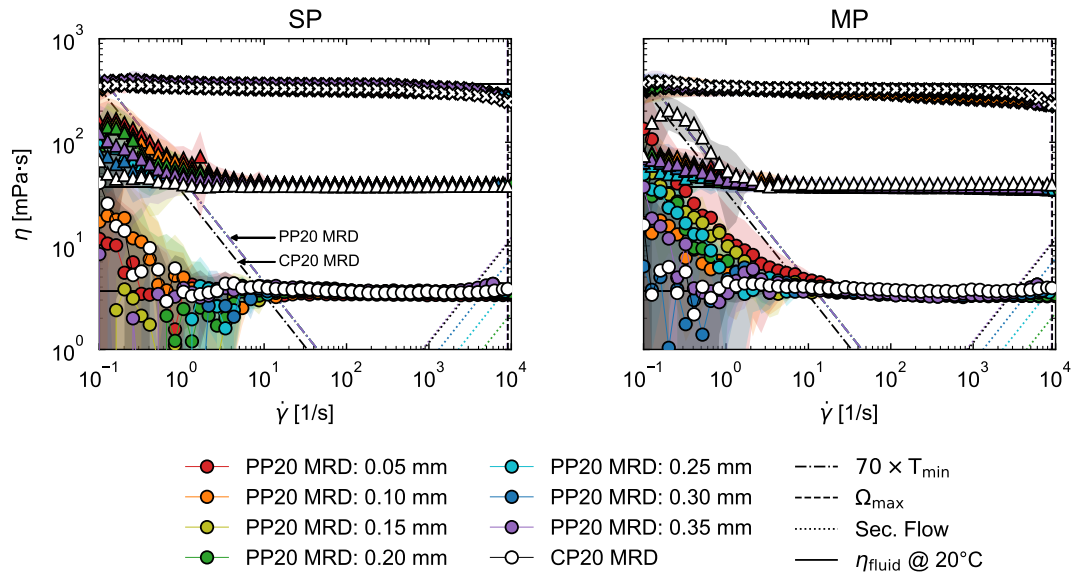


Figure 6: Viscosity curves corrected for the gap error ( $\varepsilon_{\text{SP}} = 0$  and  $\varepsilon_{\text{MP}} \approx 22.8 \mu\text{m}$ ) obtained with three Newtonian fluids: Cal. Oil (circular markers), 75.20Gly (triangular markers) and 93.05Gly (cross markers), on either bottom plate: (left) SP and (right) MP. Data gathered with the CP20 MRD and PP20 MRD (gap heights between 0.05 and 0.35 mm).

Comparing to the raw viscosity curves (Figure 3), the MP results are drastically altered,

with the correction rectifying the experimental data effectively. Thus, hereafter we will focus on elucidating the cause of the gap-error and why the CP20 MRD seems immune to the measured viscosity reduction and prone to yielding larger viscosities.

Because the SP does not show such severe gap-error symptoms, issues regarding the setting zero-gap procedure seem unlikely, as it was the same for either bottom plate. The same can be said about surface finishing issues; even if the material for either plate is different, both were acquired from the same supplier (Anton Paar) and, thus, should have somewhat similar surface characteristics (the same reasoning for slip negligibility). Assuming that the MP is straight, as we hypothesise the SP is, the most simple cause should be an inclination of the MP that leads to geometry non-parallelism.

### 3.2 Numerical analysis of the non-parallelism on standard measurements

To validate our hypothesis, we set out to model both geometries (PP20 and CP20) with varying inclinations of the bottom plate to study them numerically in a 3D simulation. The model of a non-parallel PP is very straightforward, but a CP requires some consideration. When executing the zero-gap procedure, the rheometer assumes a zero gap when contact is made between the cone and the bottom plate. In our case, we have a truncated cone with an angle of  $1.981^\circ$  and truncation height of 0.084 mm. If the inclination angle is lesser than the cone angle,  $\varphi < \beta$ , contact is made at the truncation radius,  $R_t$ . On the other hand, if  $\varphi > \beta$ , contact is made on the outer radius of the cone,  $R$ , just like a PP geometry. When the inclination is equal to the cone angle,  $\varphi = \beta$ , both models are valid as contact is made along a radial segment. Figure 7 shows schematics of the modelled PP and CP geometries (not to scale).  $h_c$  is the commanded gap, or the truncation height in the case of the CP (0.084 mm), and the radius for both geometries was  $R = 20$  mm (PP20 and CP20).

The fluid flow was then calculated in COMSOL MultiPhysics, solving for the laminar, incompressible and isothermal flow of a Newtonian fluid of equal characteristics to the Cal. Oil at  $20^\circ\text{C}$  (Table 1). The steady state equations for conservation of mass and momentum are solved:

$$\rho(\mathbf{u} \cdot \nabla) \mathbf{u} = -\nabla p + \eta \nabla^2 \mathbf{u} + \mathbf{F}, \quad (12)$$

$$\nabla \cdot \mathbf{u} = 0. \quad (13)$$

The applied boundary conditions were no-slip at the top and bottom walls. A rotational velocity,  $\Omega$ , was imposed at the top wall (the measuring system) while the bottom wall remained fixed. The sample/air interface was simplified in two ways. First, the shape of the interface was considered straight and vertical (Figure 7), while in real applications, we aim to have a perfect convex meniscus shape, whose contact angle with the solid parts is dependent on fluid surface tension. Second, the fluid/air interface was modelled as a free-slip condition for the sake of simplicity.

The mesh was constructed in COMSOL by defining it first on the top and outer walls and then using a swept mesh operation to mesh the whole volume. The whole revolution was divided into  $5^\circ$  slices, and the outer wall (fluid/air interface) was defined by partitioning the gap height, along the  $z$  direction, into 20 equal-sized elements. The

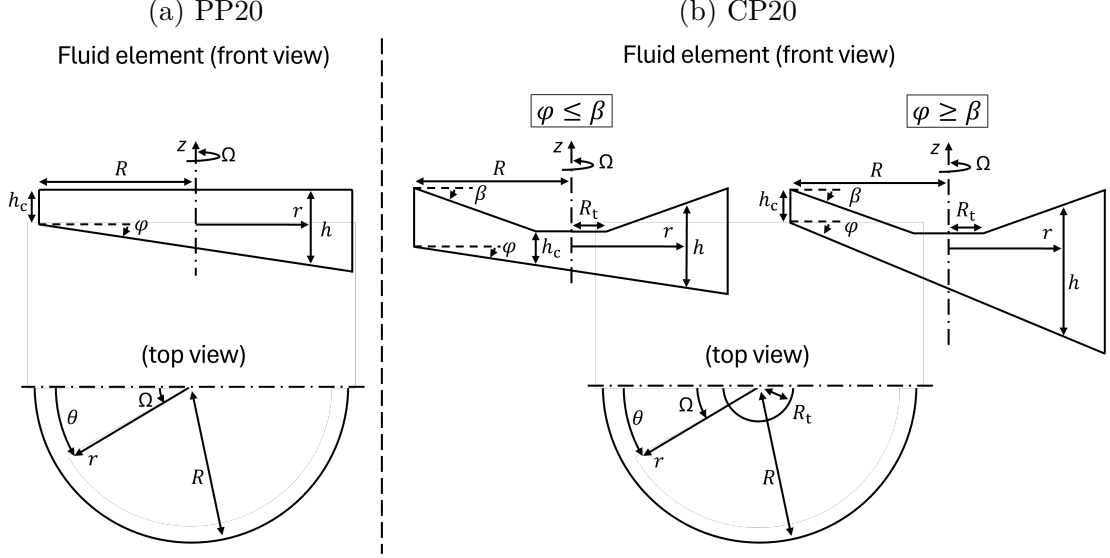


Figure 7: Schematics (not to scale) of the modelled geometries with inclined bottom plate: (a) PP and (b) CP. The CP model differs depending on the magnitude of the inclination angle,  $\varphi$ , relative to the cone angle,  $\beta$ . Cylindrical coordinate system is assumed.

top wall was divided into two sections, with a threshold diameter of 0.5 mm. On the outer region,  $0.5 \text{ mm} \leq r \leq R$ , the radial direction was divided into 30 elements, being progressively refined as we approach the outer rim of the geometry ( $r \rightarrow R$ ) to improve the resolution where we expect maximum gradients (arithmetic progression with growth factor of 5). The inner region,  $0 \leq r \leq 0.5 \text{ mm}$ , was constructed by dividing it into angular sections of  $60^\circ$  and filled with small triangular elements. Figure 8 shows the top and side views and a zoom-in on the inner region. More information regarding the mesh construction and analysis is given as supplementary material.

The models were validated by verifying the velocity profiles obtained with perfectly parallel geometries ( $\varphi = 0$ ) at a shear rate range  $10^{-1} \leq \dot{\gamma} \leq 10^4 \text{ s}^{-1}$ . The profiles never deviated from the expected Couette shape except at high shear rates when secondary flows onset, which was also accurately captured by the models (data not shown here). The viscosity "measured" by our modelled rheometer was calculated, according to Equation 1, by evaluating the torque, which was computed by integrating the wall shear stress on the top, rotating wall:

$$T = \iint_S \tau_{z\theta} r dS. \quad (14)$$

The models returned constant measured viscosity equal to the defined fluid viscosity except when secondary flows onset at high shear, which led to a measured viscosity increase (data presented as supplementary material).

Having evaluated the model's capability, we introduce the non-parallelism of the geometries by varying the inclination angle of the bottom plate,  $\varphi$ . To compare with our experimental data, the shear rate was fixed at  $\dot{\gamma} = 115 \text{ s}^{-1}$  (data point within the

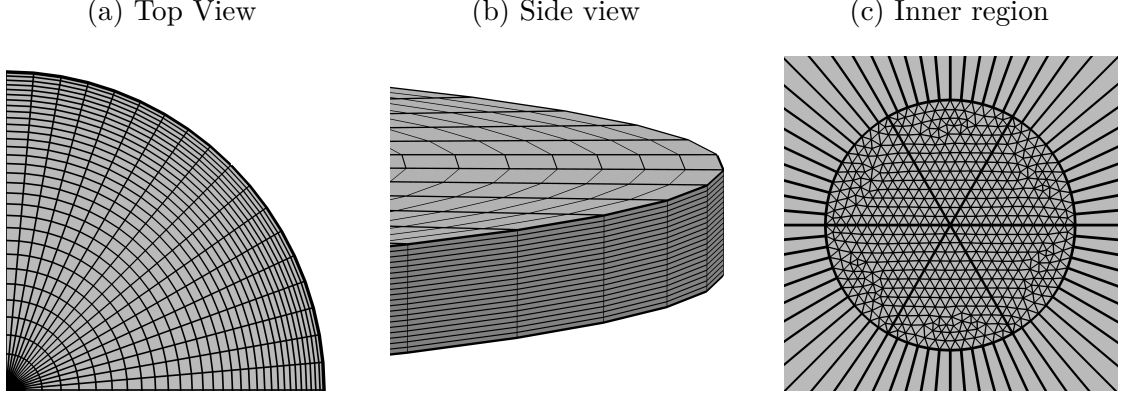


Figure 8: Domain of the fluid sample model: (a) top view, (b) side view and (c) detail of the top/bottom wall inner region.

experimental window) and twenty values for the inclination angle were tested, ten lesser than the cone angle,  $0.1^\circ \leq \varphi \leq \beta$ , and ten larger,  $\beta \leq \varphi \leq 5^\circ$ . In Figure 9 are shown the velocity profiles (velocity components:  $u_r$ ,  $u_\theta$  and  $u_z$ ) at  $r = R/2$  in opposite sides of the inclination ( $\theta = 0$  and  $\theta = \pi$ ) for five inclination angles:  $\varphi = 0, 0.1, 0.936, 1.981(= \beta)$  and  $5^\circ$ , on both geometries (only two PP20 gap heights are shown:  $h_c = 0.05$  and  $0.35$  mm).

The results show that the inclination of the bottom plate leads to divergences from the canonical Couette flow (Figure 9). Whereas the CP20 and the larger PP20 gap seem relatively unaffected by the lesser tested inclination ( $\varphi = 0.1^\circ$ ), the flow on the lesser PP20 gap is clearly altered because of the relative significance of the inclination. Despite the non-parallelism of PP geometries provoking only an increase of the local gap, the angular velocity profiles on either side of the  $0.05$  mm gap geometry are curved differently. Notably, aggravating the non-parallelism leads to interesting velocity profiles. On the one hand, at the lesser local gaps ( $\theta = 0$ ), there seems to be a velocity overshoot, noticed first for the lesser PP20 gap and then for the CP20, while on the opposite location ( $\theta = \pi$ ) negative rotational velocities are seen near the bottom wall, reaching very significant proportions particularly for the CP20 at a geometry inclination matching the cone angle ( $\varphi = \beta = 1.981^\circ$ ). To further analyse the flow, Figures 10 and 11 show, respectively, the velocity magnitude fields (at the vertical plane  $\theta = 0$ ) and the streamlines (at the horizontal plane crossing the inclined bottom plate at  $r = R_t$ ,  $\theta = 0$ ) for either geometry model and both PP20 gaps ( $h_c = 0.05$  and  $0.35$  mm), and three bottom plate inclinations.

It seems there are fundamental differences between the flow on either non-parallel geometry. Regarding the PP20, from the velocity magnitude fields we can see the inclination of the bottom plate leads to a tilt of the flow's axis of rotation, being more pronounced for smaller gaps. This explains the negative angular velocities displayed on the profiles (Figure 9) as they were gathered taking into account the geometry's axis and not the flow's. On the other hand, the flow behaviour on the non-parallel CP is more complex and, for inclinations around and larger than  $\beta$ , near the bottom of the geometry the flow counters the rotation imposed on the top wall. This phenomenon should be

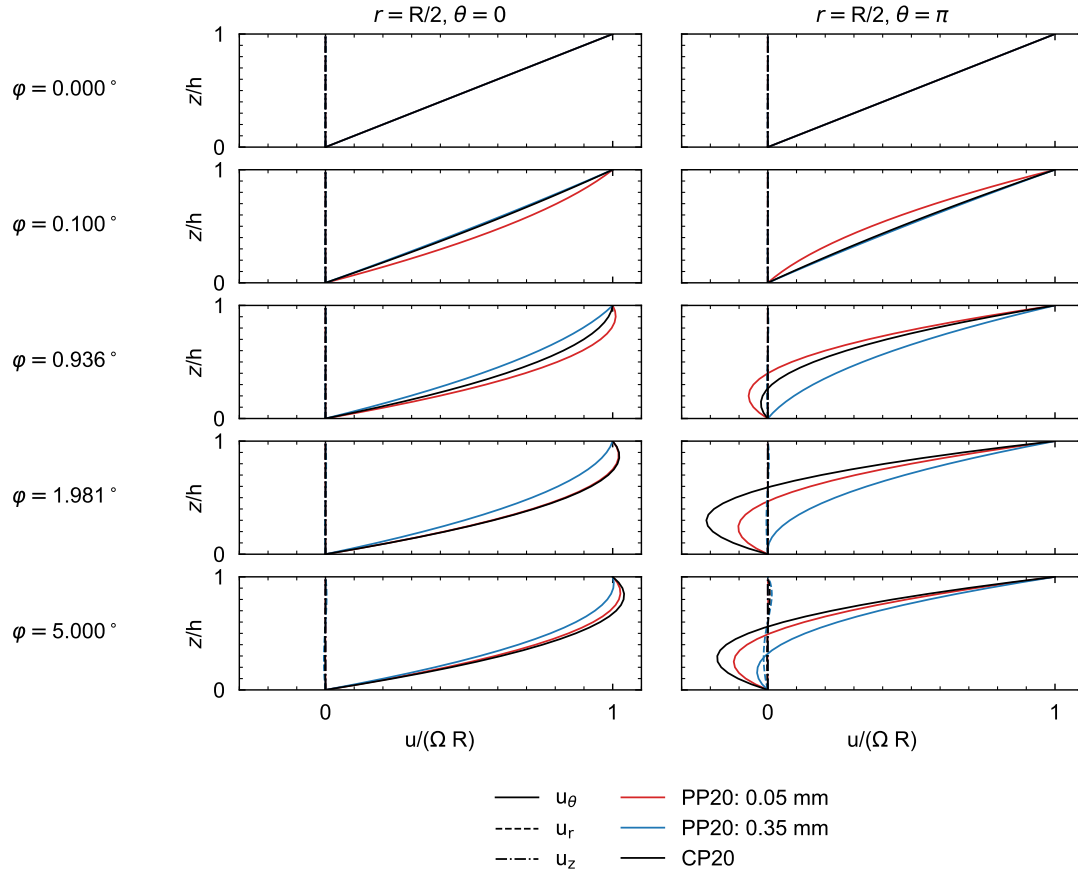


Figure 9: Velocity profiles obtained from the modelled flow of the Cal. Oil, along opposing vertical lines:  $\theta = 0$  and  $\pi$  for  $r = R/2$ , at several inclination angles ( $\varphi = 0, 0.1, 0.936, 1.981, 5^\circ$ ) in the PP20 ( $h_c = 0.05$  and  $0.35$  mm) and the CP20.

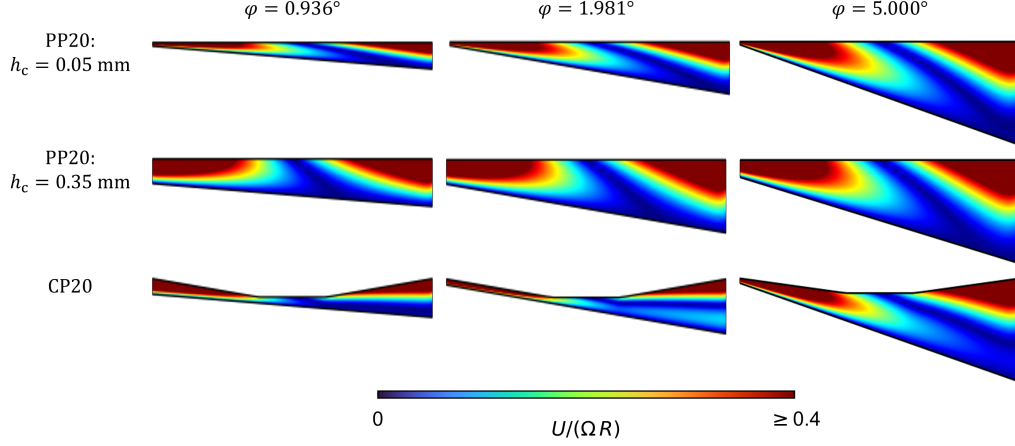


Figure 10: Velocity magnitude fields ( $U = \sqrt{u_\theta^2 + u_r^2 + u_z^2}$ ) gathered at the vertical plane  $\theta = 0$  on either geometry model and two PP gap heights ( $h_c = 0.05$  and  $0.35$  mm) for bottom plate inclinations of  $\varphi = 0.936^\circ, 1.981^\circ$  and  $5.000^\circ$ . The colorbar range was limited to 40% of the data range ( $0 \leq U \leq 0.4 \Omega R$ ) and the plots were stretched vertically (stretching factor of 5) to facilitate visualization.

due to the contraction-expansion provoked by the inclination, which has a maximum strangulation when it matches the cone angle. Increasing the inclination past this point shifts the most narrow section from the truncation radius to the outer radius, widening the contraction and, therefore, beginning to slowly dissipate the counter-rotating region.

In Figure 12 is shown the viscosity "measured" by our modelled rheometer ( $\eta_m^*$ , relative to the input Cal. Oil viscosity,  $\eta_{\text{exp}}$ , given in Table 1) with the PP20 ( $0.05 \leq h_c \leq 0.35$  mm) and CP20 geometries with varying inclination ( $0 \leq \varphi \leq 5^\circ$ ). With the PP20, the measured viscosity decreases as the inclination is increased, tending to zero as  $\varphi \rightarrow 90^\circ$  with a decreasing rate. Despite seemingly behaving as a usual gap-error on perfectly-parallel geometries, the gap-error formulation returned viscosity estimates lower than the models' input value, possibly due to the flow alterations displayed in Figures 10 and 11. This can also explain the correction of experimental data undershooting for the MP (Figure 5). Nonetheless, relatively acceptable errors ( $<10\%$ ) are still achievable through the gap-error formulation for inclinations  $\varphi \lesssim 1^\circ$ . With the CP20, the measured viscosity is initially increased until reaching a maximum when the inclination matches the cone angle, about 77% higher than the actual viscosity. This should be due to the progressive "pinching" of the contraction-expansion. On one side of the geometry,  $\theta = 0$ , the increase in inclination reduces the flow depth, leading to enhanced velocity gradients and, therefore, larger torque contributions. Whereas on the other side,  $\theta = \pi$ , there is an increase in flow depth, but the counter-rotating region is formed near the bottom wall, allowing for the maintenance of significant velocity gradients and, thus, the overall torque is increased. Increasing the inclination past the cone angle, the contraction is progressively reduced, which naturally leads to, on one hand, a reduction of the velocity gradients at the constricted section and, on the other hand, to the dissipation of the recirculation



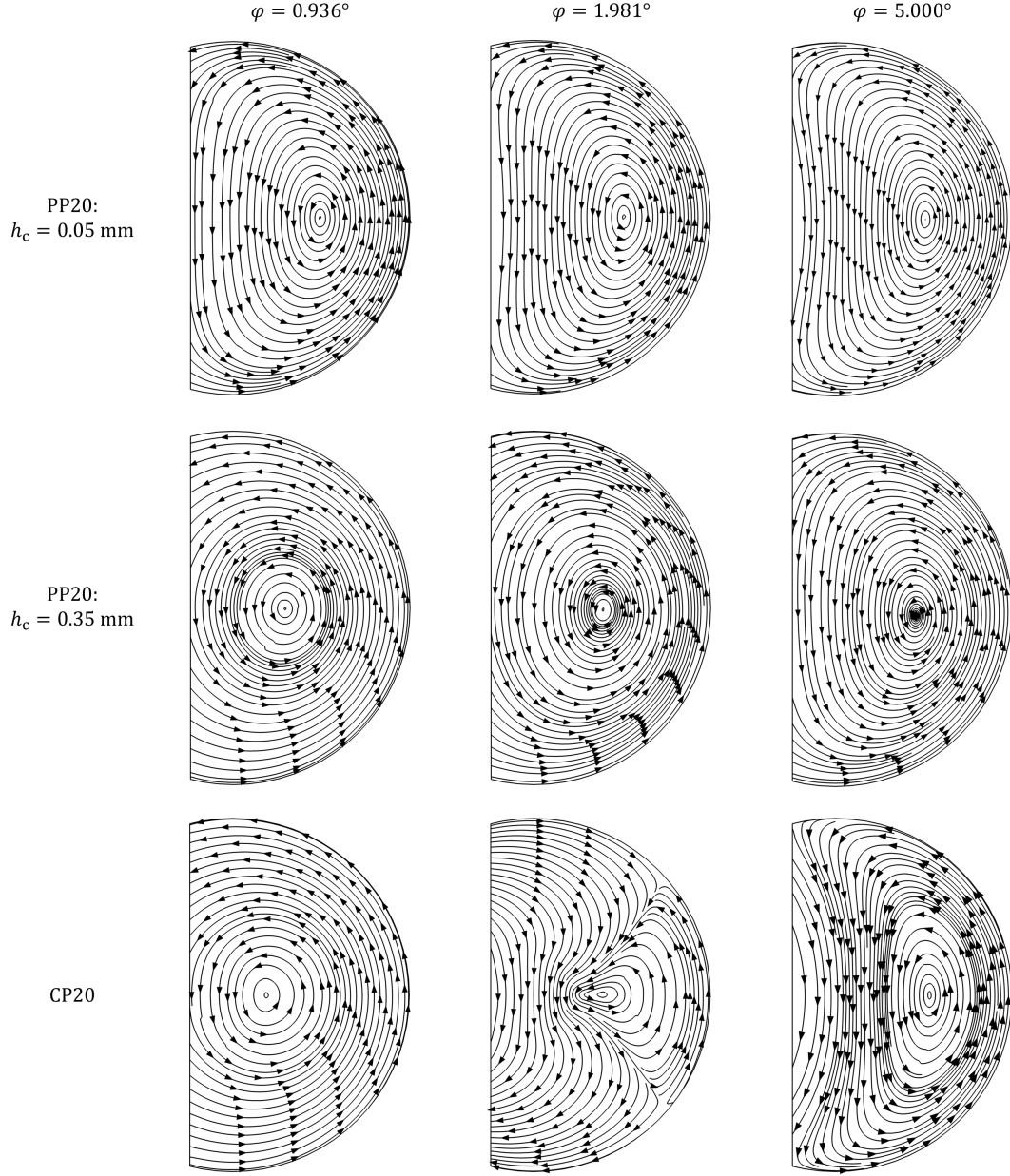


Figure 11: Streamlines gathered at an horizontal plane (crossing the inclined bottom plate at  $r = R_t$  and  $\theta = 0$ ) on either geometry model and two PP gap heights ( $h_c = 0.05$  and  $0.35$  mm) for bottom plate inclinations of  $\varphi = 0.936^\circ, 1.981^\circ$  and  $5.000^\circ$ . Imposed rotational velocity on the top wall is counter-clockwise.

region, which additionally reduces the velocity gradients, leading to a measured viscosity decrease.

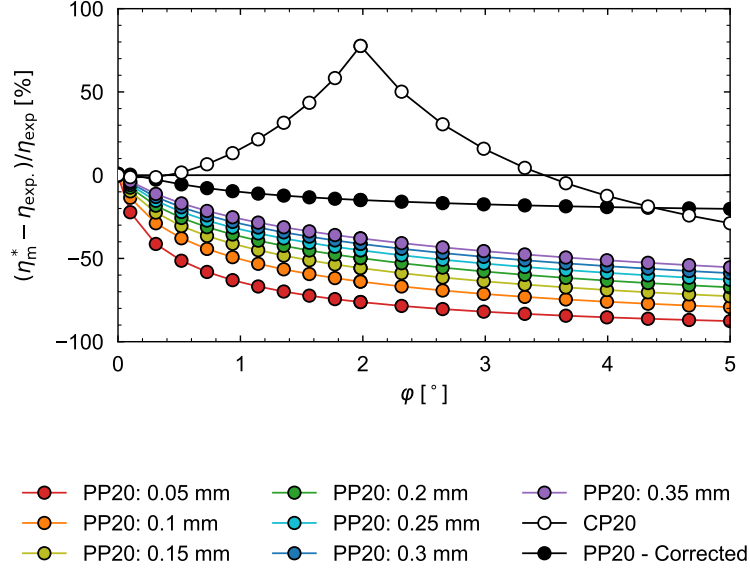


Figure 12: Modelled Cal. Oil numerical viscosity ( $\eta_m^*$ , relative to the input value,  $\eta_{exp}$ , given in Table 1) with varying inclination of the bottom plate ( $0 \leq \varphi \leq 5^\circ$ ) on the PP20 ( $0.05 \leq h_c \leq 0.35$  mm) and CP20 geometries.

These results agree with the experimental ones that showed PP20-measured viscosity decreasing with gap reduction and a slight increase in CP20-measured viscosity. A standard gap-error on perfectly parallel geometries (arising, for example, from misjudged zero-gap, due to air squeeze or other phenomena) would only lead to a viscosity decrease (this was also evaluated for our models and is presented as supplementary material). Thus, according to the previous experimental data we can infer that the bottom MP is likely slightly inclined. Fitting of the numerical viscosity, a gap-error of  $\varepsilon = 22.8 \mu\text{m}$  should be estimated from an inclination between  $0.10 < \varphi < 0.31$ , but, if so, according to Figure 12, the CP-viscosity increase should not be noticeable, contrary to our experimental observations. Other surface defects could have a similar effect on experimental results; however, the issue may lie not with the quality of the plate's surface but with its coupling to the magnetorheological cell. Looking again at Figure 1(b2), we can observe that the MP is fixed to the cell via two screws and either dimensional issues with the screws themselves or surface defects on the bottom of the plate where contact is made could be responsible for this inclination.

Geometry non-parallelism can be predicted and corrected fairly well for PP geometries through the gap-error formulation and viscosity data at multiple gap heights. However, as far as we know, there is no equivalent approach for CP geometries. The flow dynamics can become relatively complex, and the measurements can return unexpected results as we generally assume geometry non-parallelism to result similarly to a general gap error.

From this numerical work, we can gather that reasonably acceptable errors ( $<10\%$ ) can be obtained for standard measurements with a CP20 geometry for inclinations:  $\varphi \lesssim 1^\circ$ . For  $3^\circ \lesssim \varphi \lesssim 4^\circ$  the CP also returns small errors, but the divergence from the canonical flow can significantly impact the behaviour of the used sample. Until now, we have focused on single-phase Newtonian fluids, but measurements of more complex samples may be affected differently. In the following Sections, we shall discuss the impacts of geometry non-parallelism on magnetorheological measurements.

### 3.3 Experimental magnetorheological measurements

Measurements were performed to evaluate the setup capability of generating a measurable magnetorheological response and how the bottom plate and used geometry impacts the results. To this end we employed the Newtonian blood analogue — NBa (composition and expected density and viscosity in Table 1).

Initially, the analogue’s viscosity curves were obtained without particles and no magnetic field application, using both geometries and bottom plates. Tests were conducted with four different gap heights for the PP, ranging from 0.05 to 0.35 mm. The resulting viscosity curves are illustrated in Figure 13. Again, the data is similarly affected by the gap-error, showing decreased PP-measured viscosity with gap height reduction and increased CP-measured viscosity. On the other hand, the NBa seems more sensitive to low-shear issues than the Cal. Oil, particularly for larger gaps on the MP, which could be due to the analogue’s more significant surface tension.

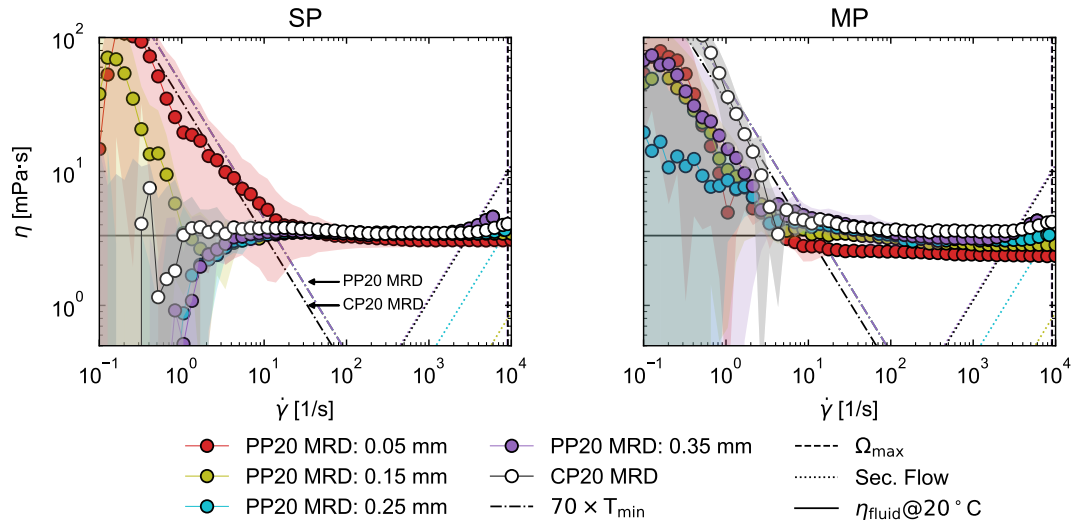


Figure 13: Viscosity curves obtained with the Newtonian blood analogue (NBa), on either bottom plate: (left) SP and (right) MP. Data gathered with the CP20 MRD and PP20 MRD (gap heights between 0.05 and 0.35 mm). No magnetic field was applied ( $B = 0$ ).

The magnetorheological steady shear measurements were conducted with the NBa seeded with three concentrations of the M270 particles: 5, 10 and 15 wt%, which

are equivalent to volume fractions of  $\phi \approx 3.4, 6.9$  and  $10.6$  vol% (corresponding to dilute/semi-dilute suspensions<sup>17</sup>). The shear rate was kept constant at  $\dot{\gamma} = 500 \text{ s}^{-1}$  (within the experimental window of the unseeded NBa) and the magnetic field intensity was varied up to  $B \leq 720 \text{ mT}$ . The measurements were conducted on the MP, with both geometries (PP20 MRD and CP20 MRD). With the PP20 MRD, the fluid viscosity was measured at different gap heights:  $0.05 \leq h_c \leq 0.35 \text{ mm}$ , (left column of Figure 14), and the data gathered at an intermediate gap,  $h_c = 0.15 \text{ mm}$ , was corrected for the gap-error  $\varepsilon = 22.8 \text{ }\mu\text{m}$  (right column of Figure 14).

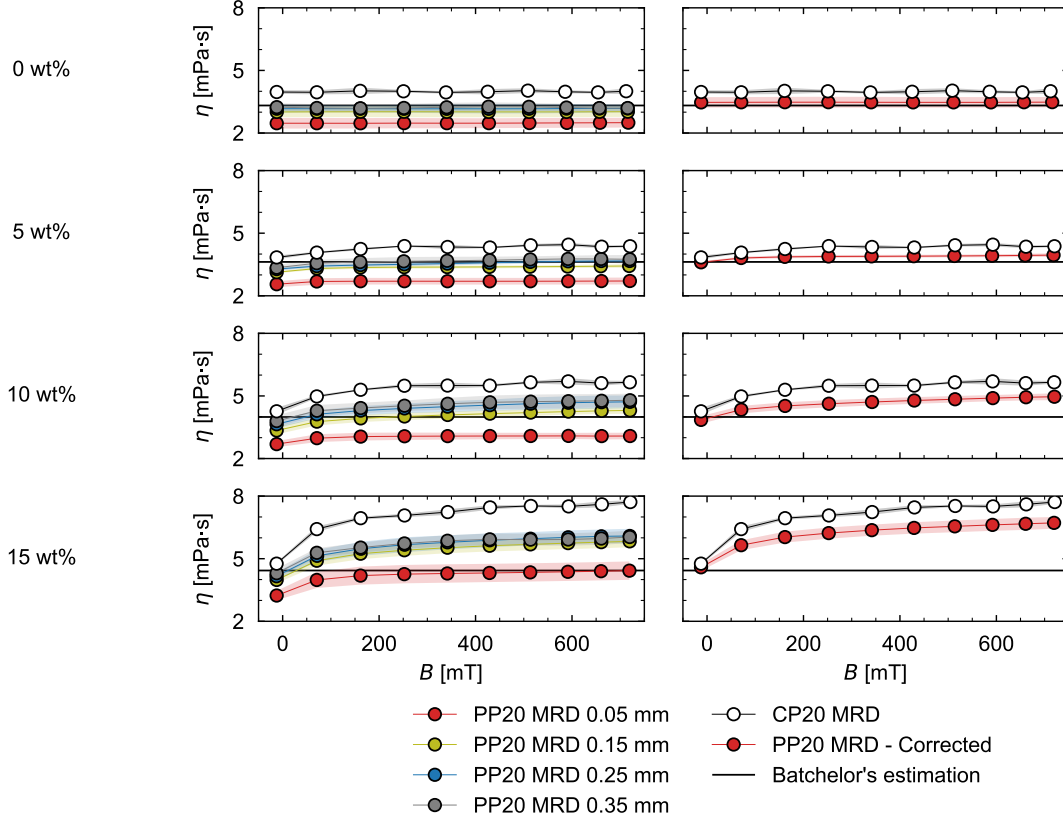


Figure 14: Viscosity data (at  $\dot{\gamma} = 500 \text{ s}^{-1}$ ) of the NBa seeded with magnetic particles at different mass concentrations (0, 5, 10 and 15 wt%), on the MP with varying magnetic field density ( $B \leq 720 \text{ mT}$ ). Data gathered with the CP20 MRD and PP20 MRD (gap heights between 0.05 and 0.35 mm). In the right column, the PP20 data gathered at  $h_c = 0.15 \text{ mm}$  is shown corrected for the gap-error ( $\varepsilon = 22.8 \text{ }\mu\text{m}$ ). Horizontal black lines correspond to Batchelor's estimated viscosity of the seeded NBa at  $20^\circ\text{C}$  (Equation 16).

Before discussing the results, we address some possible experimental issues. Evaluating the Peclet, Reynolds and Stokes numbers, the results to Equations 8-10 are, respectively:  $1/Pe \approx 4.7 \times 10^{-5}$ ,  $Re_p \approx 3.1 \times 10^{-4}$  and  $St \approx 1.0 \times 10^{-4}$ , which are  $\ll 1$ , meaning

we can disregard Brownian and inertial effects. Regarding particle sedimentation, the settling velocity in a dilute system can be given by:

$$V_s = (1 - 6.55\phi) \frac{(d_p/2)^2 \Delta\rho g}{18\eta}, \quad (15)$$

where the term  $(1 - 6.55\phi)$  accounts for the hindered backflow of the continuous phase due to the presence of the particles,  $\Delta\rho$  is the density difference between dispersed and continuous phases and  $g$  is the gravitational acceleration<sup>30</sup>. The resulting sedimentation velocities are, for 5, 10 and 15 wt% concentrations, respectively:  $V_s \approx 0.55, 0.39$  and  $0.22$   $\mu\text{m/s}$ , which may be significant given our small gap heights, even if the total measurement time was relatively short (200 s). However, because the magnetic field is aligned with the gap, the magnetic dipole forces will counter the gravitational effects, further hindering the particle sedimentation.

Looking at the results obtained without magnetic field application,  $B = 0$  there is an increase in viscosity with magnetic particle concentration, which is reasonably predicted by Batchelor's expression<sup>31</sup>:

$$\eta^* = \eta (1 + 2.5\phi + 6.2\phi^2), \quad (16)$$

(shown in Figure 14 as horizontal black lines) where  $\phi$  is the particle volume fraction.

Regarding the magnetic field effects, the results present the expected response: an increase in viscosity is noted with enhanced magnetic field density, which is more significant the larger the particle concentration. This is because the particle-chains formed from the magnetic-induced dipole interactions are aligned (with the field) perpendicular to the flow direction, hindering it, provoking an additional torque and, therefore, an increase in measured viscosity. There is a discrepancy between the PP20 and CP20 results, with the latter always presenting larger measured viscosities, and may seem dependent on the particle concentration and the magnetic field density. Nevertheless, this could be the same effect of the bottom plate inclination as previously discussed, because the relative error between the two geometries remained relatively constant ( $(\eta_{\text{CP}} - \eta_{\text{PP}})/\eta_{\text{CP}} \approx 13.5\%$ ), it just becomes visually prominent due to the viscosity increase with magnetorheological enhancement.

It is worth mentioning that because we employed smooth geometries, our data is likely affected by apparent slip of the dispersed phase which would significantly reduced the measured magnetorheological response<sup>18,32</sup>. As such, these results serve only to verify that the employed setup is able to generate a significant magnetorheological response and to compare between the discussed geometries. We do note that inhibiting slip, either through roughened or detailed geometries, should return a much stronger magnetorheological behaviour with measured viscosities perhaps up to orders of magnitude larger.

Lastly, and on a side note, heating effects from the magnetic field generation were observed from a very slight temperature rise at the largest field densities, but it should not have significantly affected the results ( $< 0.3^\circ\text{C}$ ).

### 3.4 Numerical analysis of the non-parallelism on magnetorheological measurements

As the SP is not applicable for magnetorheology, decoupling the effects of the MP's inclination on this type of measurement was not possible. Thus, the flow of magnetised particles seeded in the NBa was evaluated numerically using the rheometer models. The experimental procedure would ideally be replicated to assess the impact of non-parallelism on bulk viscosity measurements and particle chain dynamics accurately. However, the number of modelled particles needed for this replication results in extensive simulations that are, unfortunately, beyond our current computational capabilities.

Taking a different approach, the effects of geometry non-parallelism on particle-chain behaviour can be assessed by evaluating only a few chains with a small number of particles placed strategically in the flow. We placed particle chains at half the geometry radius:  $r = R/2$  at four equally-distanced angular positions:  $\theta \in [0, \pi/2, \pi, 3\pi/2]$ . To have coherency between the geometries, the effective gaps at  $r = R/2$  were equal:  $h_c^{\text{PP20}} = h^{\text{CP20}}|_{R/2} = (R/2) \tan(\beta)$ .

COMSOL's *particle tracing for fluid flow* module was used. The forces considered to be acting on the particles were the viscous drag due to the fluid flow and dipole-dipole interactions due to particle magnetisation. Particle sedimentation has already been discussed in the previous Section and again addressing Brownian motion, [Melle et al.](#) defined an adimensional ratio between magnetic and thermal energies:

$$\lambda = \frac{\mu_0 \mu_f m^2}{16 \pi (d_p/2)^3 k_B T}, \quad (17)$$

where  $k_B$  is the Boltzmann constant and  $T$  is the temperature, which we defined as 20°C. Using the M270 saturation magnetisation<sup>22</sup> ( $m_{\text{sat.}}^{\text{M270}} = 6.4 \times V_p \rho_p [\text{Am}^2]$ , where  $V_p$  is the particle volume), we obtain  $\lambda \approx 32000 \gg 1$ , meaning the magnetic effects dominate over Brownian motion.

Viscous drag was computed using COMSOL's in-built Stokes drag force:

$$\mathbf{F}_d = 3 \pi \eta d_p (\mathbf{u}_f - \mathbf{u}_p), \quad (18)$$

where  $(\mathbf{u}_f - \mathbf{u}_p)$  is the particle velocity ( $\mathbf{u}_p$ ) relative to the fluid ( $\mathbf{u}_f$ ). The dipolar forces were computed through particle-particle interactions following the expression given by [Melle et al.](#):

$$\mathbf{F}_{a,ij} = \frac{3 \mu_0 \mu_f m^2}{4 \pi r_{ij}^4} \left[ \left( 1 - 5 (\hat{n} \cdot \hat{r}_{ij})^2 \right) \hat{r}_{ij} + 2 (\hat{n} \cdot \hat{r}_{ij}) \hat{n} \right], \quad (19)$$

where  $\mu_0$  and  $\mu_f$  are the vacuum and fluid permeabilities, respectively (the latter being the relative permeability and considered  $\mu_f = 1$ ). This expression assumes all particles are equally affected by the external field, i.e., their magnetisation is identical and aligned with the magnetic field, which, in this case, was considered uniform and perpendicular to the flow direction, as in the magnetorheological cell. The magnetic force depends on two

vector components: the magnetic moment  $\mathbf{m}$  and the inter-particle distance<sup>ii</sup>  $\mathbf{r}_{ij}$  (with magnitude  $m$  and  $r_{ij}$ , and adimensional directions  $\hat{\mathbf{m}}$  and  $\hat{\mathbf{r}}_{ij}$ , respectively).

The particles are considered hard spheres and, to approximate this behaviour, a repulsive excluded-volume force was applied<sup>33,34</sup>:

$$\mathbf{F}_{r,ij} = 2 \frac{3 \mu_0 \mu_f m^2}{4 \pi d_p^4} \exp \left[ -30 \left( \frac{r_{ij}}{d_p} - 1 \right) \right] \hat{\mathbf{r}}_{ij}. \quad (20)$$

Aligned with the field, the excluded volume force perfectly balances the magnetic attraction when two particles are in mechanical contact ( $r = d_p$ ). Whereas, when the inter-particle distance is  $r = 1.1 d_p$ , the excluded-volume force is approximately 14 times smaller than the magnetic attraction force, not provoking unwanted forces in other surrounding particles<sup>34</sup>. Both these forces were computed as particle-particle interactions, and, therefore, we define a general magnetic force acting on the particles as:

$$\mathbf{F}_{m,ij} = \mathbf{F}_{a,ij} + \mathbf{F}_{r,ij}. \quad (21)$$

In truth, the presence of the particles induces changes in the fluid flow. But, despite COMSOL allowing for the coupling of different physics, this would further complicate the model. Therefore, we opted only to evaluate the effects of the fluid on the particle chains and disregard the inverse phenomenon. Furthermore, as we have already simplified the problem to analyse only a few chains, these effects on the total torque measurement would be negligible and not representative of the impact on a real measurement. The particle boundary condition forced the particles that collide with the geometry walls or the simplified fluid/air interface to adhere to them with no slip, reducing their velocity to zero. As we are only interested in the behaviour of a general particle chain for a qualitative analysis, we could alter the particle diameter to reduce the required number of particles per chain and their magnetisation, which, when decreased, allows lesser magnetic forces to facilitate convergence. To have a clear idea of the possible effects of the geometrical changes on the particle chains, we wanted to set the system properties so that the chains remain unbroken in the perfectly parallel geometries while keeping the models relatively light. Therefore, we had an interplay between particle size, particle magnetisation and flow velocity, where small particles, i.e., large chains<sup>34</sup>, low magnetisation and large shear rates led to chain break. We performed simulations of a single chain on the parallel CP20 to test the limits of these characteristics. The particle diameter was varied between 35 and 16  $\mu\text{m}$ , leading to chains of 4 to 10 particles<sup>iii</sup> and the shear rate ranged from 0.01 to 1  $\text{s}^{-1}$ , guaranteeing that the particles are capable of effectively following the flow (for  $d_p = 35 \mu\text{m}$ , from Equation 10:  $St \approx 3.3 \times 10^{-5} \ll 1$ ). The magnetisation was progressively decreased using a factor,  $1 \leq C_m \leq 50$ , such that the tested magnetisation was:  $m^* = m_{\text{sat.}}^{\text{M270}} / C_m$ . From these simulations, three behaviours were observed: a) the chain remained unbroken, b) the chain undergoes subdivision (including combinations

<sup>ii</sup>The inter-particle distance is the vector between particle centres.

<sup>iii</sup>The number of particles in each chain was calculated by rounding down (to the nearest integer) the required particle number to span the local gap height:  $n = \lfloor h/d_p \rfloor$ , where  $d_p$  is the modelled particle diameter.



of minor chains and isolated particles), and c) the chain completely breaks down into individual particles. Examples of these behaviours are showcased in Figure 15, and the results can be seen in Figure 16.

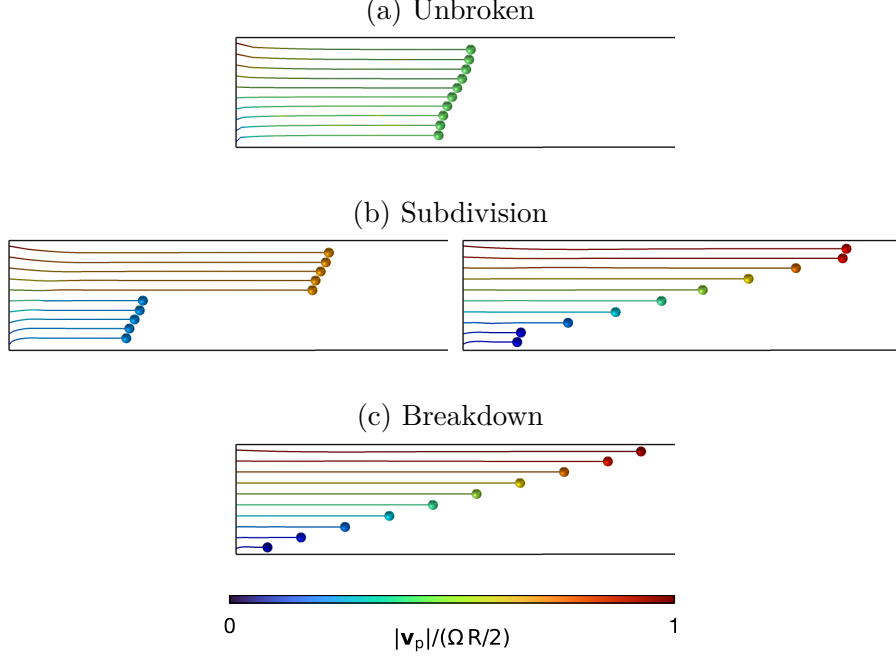


Figure 15: Magnetised-particle chain ( $d_p = 16 \mu\text{m}$ ,  $n_p = 10$ ) on the CP geometry model (without bottom plate inclination) with imposed shear rate  $\dot{\gamma} = 1 \text{ s}^{-1}$  with varying magnetisation factor: (a)  $C_m = 5$ , (b)  $C_m =$  (left) 10 and (right) 20, (c)  $C_m = 30$ . The particles are initially placed in a vertical uniform distribution (vertical line segment on the left, of length,  $R/2 \tan(\beta)$ ) and the shown images were taken at  $t = 4 \text{ s}$ . Flow is left to right.

Usually, a Mason number,  $Mn$ , that describes the ratio between viscous and magnetic effects is used to identify the transitions in chain dynamics<sup>33</sup>, and a multitude of different formulations have been previously employed<sup>33–36</sup>. With our data, the Mason number defined by [de Gans et al.](#) suitably predicts the complete breakdown of the chains when approaching unity:

$$Mn = \frac{128 \pi^2 (d_p/2)^6 \eta \dot{\gamma}}{\mu_0 \mu_f m^{*2}} = 1, \quad (22)$$

which can be seen, plotted in black, in Figure 16. From its definition, this Mason number seems dependent on the particle size, but having that:

$$M_{\text{sat.}}^{\text{M270}} = 6.4 \times \rho_p = m_{\text{sat.}}^{\text{M270}} / V_p [\text{A/m}], \quad (23)$$

and, therefore,  $M^* = M_{\text{sat.}}^{\text{M270}} / C_m$ , we can simplify the Mason number to:

$$Mn = \frac{72 \eta \dot{\gamma}}{\mu_0 \mu_f M^{*2}}. \quad (24)$$

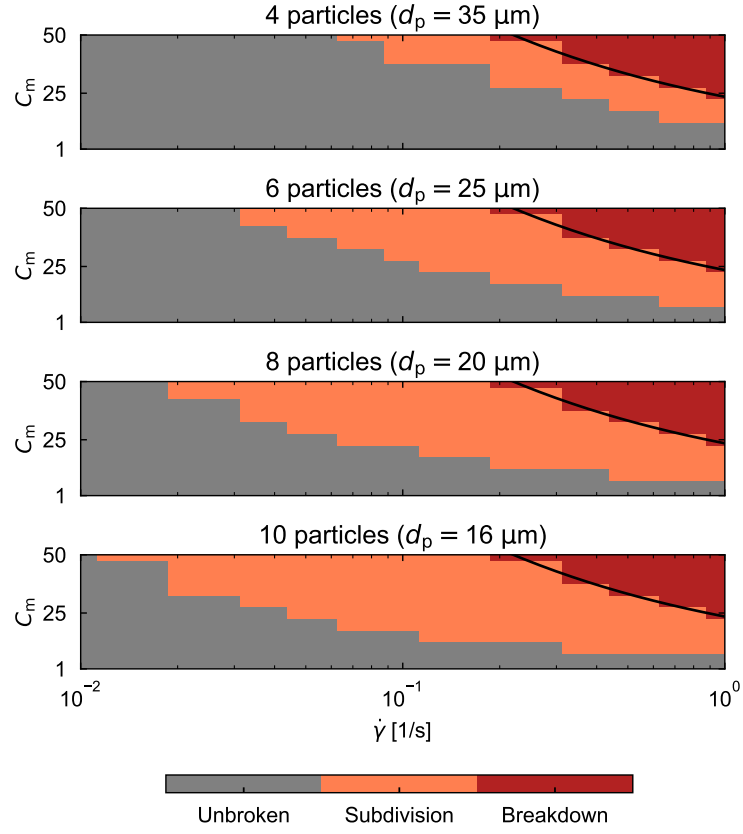


Figure 16: Magnetised-particle chain behaviour under steady shear in a planar geometry with varying particle diameter (number of particles per chain), particle magnetisation (through the scaling constant  $C_m$ ) and shear rate ( $\dot{\gamma}$ ). In black, chain complete-breakdown prediction through the Mason number defined by [de Gans et al.](#):  $Mn = 1$ .

As such, the chain complete breakdown is only dependent on the fluid properties, which were set to the NBa's, the shear rate and the particle magnetisation, independent of the number of particles and their size, as corroborated by the results in Figure 16. The same cannot be said about chain subdivision, which has a clear dependence on particle number, making larger chains easier to break. We have yet to find a second Mason number that accurately predicts our chain subdivision, but it is an issue that is out of the scope of this work.

We could select a shear rate and particle magnetisation through the gathered data that minimised the computational effort while maintaining unbroken chains in the perfectly parallel geometries. It is pertinent to have the same defined shear rate (rim shear rate,  $\dot{\gamma}(R)$ ) for both geometries, similar to the experimental procedure and, having determined the PP gap height as  $h_c = R/2 \tan(\beta)$ :

$$\dot{\gamma}(R) = \dot{\gamma}_{PP}(R) = \dot{\gamma}_{CP}(R) \Leftrightarrow \frac{R}{R/2 \tan(\beta)} \Omega_{PP} = \frac{1}{\beta} \Omega_{CP} \Leftrightarrow \Omega_{PP} \approx \frac{\Omega_{CP}}{2}. \quad (25)$$

Thus, at the defined location for chain deployment ( $R/2$ ), the local shear rate on the PP geometry:

$$\dot{\gamma}_{PP}(R/2) = \frac{R/2}{R/2 \tan(\beta)} \Omega_{PP} = \frac{\dot{\gamma}(R)}{2}. \quad (26)$$

This dictates a parameter choice where, for the chosen particle number and magnetisation parameter  $C_m$ , the chains remain unbroken at two local shear rates:  $\dot{\gamma}(R)$  and  $\dot{\gamma}(R)/2$ . We opted for chains with only 4 particles ( $d_p = 35 \mu\text{m}$ ) and a rim shear rate of  $\dot{\gamma}(R) = 1 \text{ s}^{-1}$ , having, thus, the maximum particle magnetisation factor before chain subdivision:  $C_m = 10$  (particle magnetisation:  $M^* = 6.4 \rho / C_m = 1024 \text{ A/m}$ ).

Before heading to the results, it is worth mentioning that the characteristics of the geometries are significant to the chain dynamics. The CP's constant shear rate along the radius (when disregarding the truncated region) corresponds to the maximum shear rate induced on the PP (at the rim), therefore, for chains of equal length with an arbitrarily imposed rim shear rate, the CP is more likely to break the chains. On the other hand, the CP gap height depends on the radial position, which leads to smaller, harder to break chains as we approach the centre. As such, an interplay between varying shear rate (on the PP) and chain length (on the CP) can diverge the magnetorheological results of either geometry.

In Figure 17 are shown the particle trajectories in both geometries (without bottom plate inclination) at time  $t = 650 \text{ s}$  (the trajectories at other times,  $t = 70$  and  $200 \text{ s}$ , are not included here for the sake of conciseness, but are provided as supplementary material). The chains remain unbroken, travelling along the plane  $r = R/2$  on either geometry, but moving faster on the CP20, where they are subject to a larger rotational velocity ( $\Omega_{CP} \approx 2 \Omega_{PP}$ ).

Introducing a bottom plate inclination of  $\varphi = 1^\circ$  (the maximum for acceptable viscosity measurements), the analogous results are shown in Figure 18. Before discussing the chain dynamics, the introduced geometry non-parallelism affects the number of particles in each chain. For the PP, it increases particle number from 4 in each chain to chains of 7, 9 and

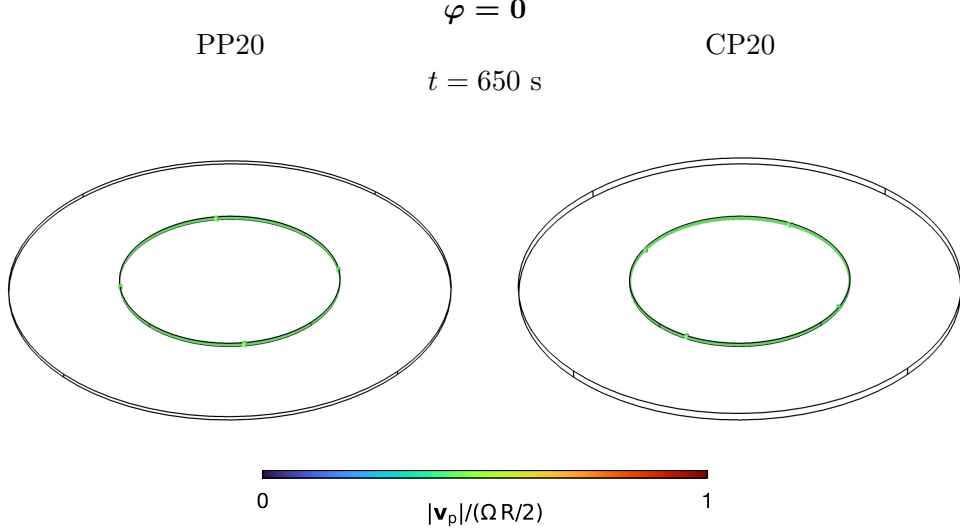


Figure 17: Magnetised-particle trajectories ( $d_p = 35 \mu\text{m}$  and  $M^* = 1024 \text{ A/m}$ ) on the (left) PP20 and (right) CP20 models (without bottom plate inclination:  $\varphi = 0$ ) with imposed shear rate  $\dot{\gamma} = 1 \text{ s}^{-1}$  at time  $t = 650 \text{ s}$ .

12 particles. For the CP, because the inclination is lesser than the cone angle ( $\varphi < \beta$ ), the gap is reduced at the constrained region,  $\theta = 0$ , (see Figure 7) before increasing as we descend along the inclination, which leads to chains of 3, 6 and 8 particles.

Considering the PP results (left column of Figure 18), initially only the largest chain, of 12 elements, subdivides, consequently separating. Compared to the particle flow on the parallel geometry (Figure 17), the chains begin to diverge from the  $R/2$  plane because the inclination of the geometry also leads to an inclination of the rotational axis. This becomes more evident as we move forward in time, particularly for  $t = 650 \text{ s}$ , where the trajectories of most chains overlap. There are some additional observations regarding wall interactions. Because the intermediate chains (of 9 particles at  $\theta = \pi/2$  and  $3\pi/2$ ) do not subdivide, while travelling along the tilted geometry, they collide with the bottom wall and lose the particle that adheres to it. With a similar behaviour, the subdivided portion of the largest chain closest to the bottom wall also collides with it, but instead of further subdividing or losing the contact particle, because the local shear rate is not sufficiently strong, the whole chain is stuck to the wall.

Considering the CP (right column of Figure 18), only the smaller chain of 3 elements remains unbroken. As the imposed rotational velocity is larger in this geometry, the enlarged shear rate leads to their subdivision despite the intermediate chains being three elements smaller than on the PP. In this case, because the intermediate chains are also broken, the three subdivided portions closest to the bottom wall stick to it when contact is made. Despite significantly altering the flow, this slight inclination does not reveal the counter-rotating region near the bottom wall. However, increasing the inclination angle to  $\varphi = \beta = 1.981^\circ$  does generate a much stronger recirculation region (see Figure

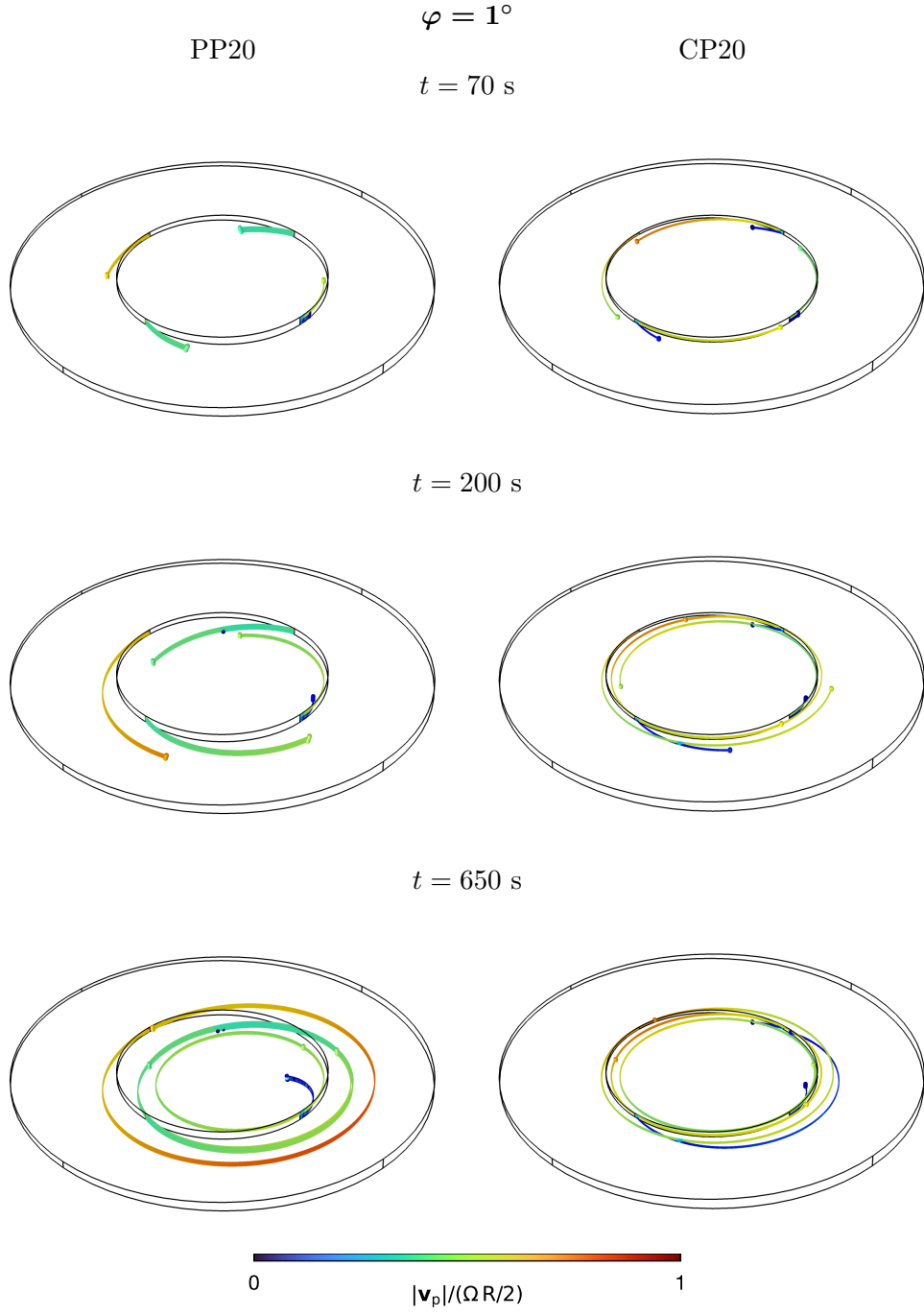


Figure 18: Magnetised-particle trajectories ( $d_p = 35 \text{ }\mu\text{m}$  and  $M^* = 1024 \text{ A/m}$ ) on the (left column) PP20 and (right column) CP20 models with a bottom plate inclination of  $\varphi = 1^\circ$ , with imposed shear rate  $\dot{\gamma} = 1 \text{ s}^{-1}$  at different times ( $t = 70, 200$  and  $650 \text{ s}$ ).

9), which significantly affects the chain dynamics. For the sake of clarity, the particle trajectories for  $\varphi = \beta$  are not shown here but are presented as supplementary material.

The bottom plate inclination calls for larger chains, which are easier to break, but the subdivided portions may be close in size to the original chains we ought to have in the perfectly parallel geometries. However, the issue with the magnetorheological measurements is not the chain size directly but the consequent chain velocity. Near the measuring geometry (top wall in this case), the closer the chain velocity is to the flow velocity, the lesser the influence on the measured torque and, therefore, the lesser the magnetic influence is felt. The particle trajectories shown in Figures 17 and 18 were plotted with a colour scheme in which the particle velocity is scaled with the maximum velocity at deployment ( $\Omega R/2$ ), which allows us to see that the particles near the measuring plate/cone (on top) have a larger velocity on the tilted geometries than on the parallel ones, which will reduce the magnetically-induced measured-viscosity increase.

## 4 Conclusions

In this work we set out to evaluate the suitability of an experimental setup for steady shear magnetorheological measurements of whole blood. An experimental campaign was conducted with Newtonian fluids in two planar geometries specially designed for magnetorheological measurements, one parallel-plate (PP20 MRD) and one cone-plate (CP20 MRD), and on two bottom plates, one for standard measurements (SP) and one for magnetic testing (MP).

It was found that the rheometer's minimum torque multiplied by a  $70\times$  factor reasonably delimited low shear errors and the apparent shear-thickening at high shear was accurately predicted by the onset of secondary flows. On the MP we encountered a dependence of the PP-measured viscosity with gap height, returning lower viscosities as the gap is reduced, and larger CP-measured viscosities with this bottom plate than with the SP. The gap-error formulation<sup>15</sup> effectively corrected the PP-measured viscosity data and the error itself was found to be around  $\varepsilon \approx 22.8 \mu\text{m}$  and most probably provoked by an inclination of the MP.

Numerical models of non-parallel geometries corroborated the experimental results, pointing towards an MP inclination between  $0.10 < \varphi < 0.31^\circ$ . The numerical work also revealed that the geometry non-parallelism can lead to notable flow alterations, particularly for CP geometries which essentially give rise to contraction-expansion flow and may lead to the emergence of counter-rotating regions as the inclination approaches the cone angle.

Magnetorheological measurements were also conducted with a Newtonian blood analogue seeded with magnetic particles and the results showed a viscosity increase with particle concentration and magnetic field density. The flow of a few particle chains was modelled and it was observed that geometry non-parallelism can significantly affect magnetorheological measurements, seemingly diminishing the magnetic effects.

## Supplementary material

As supporting material we present: preliminary measurements, a description and discussion on the mesh employed on the numerical work, numerical estimations of the effects of a general gap-error on viscosity measurements with parallel geometries, and trajectories of magnetised particles in perfectly parallel geometries and with a bottom plate inclination equal to the angle of the employed Cone-Plate (obtained numerically).

## Acknowledgements

This work was financially supported by national funds through the FCT/MCTES (PID-DAC), under the project PTDC/EME-APL/3805/2021 (DOI 10.54499/PTDC/EME-APL/3805/2021), LA/P/0045/2020, UIDB/00532/2020 and UIDP/00532/2020, and the program Stimulus of Scientific Employment, Individual Support-2020.03203.CEECIND.

## References

- [1] H. H. Billett. Hemoglobin and Hematocrit. *Clinical Methods: The History, Physical, and Laboratory Examinations*. 3rd edition, 1990.
- [2] A. Z. Valant, L. Žibera, Y. Papaharilaou, A. Anayiotos, and G. C. Georgiou. The influence of temperature on rheological properties of blood mixtures with different volume expanders—implications in numerical arterial hemodynamics simulations. *Rheologica acta*, 50:389–402, 2011.
- [3] M. Zborowski, G. R. Ostera, L. R. Moore, S. Milliron, J. J. Chalmers, and A. N. Schechter. Red Blood Cell Magnetophoresis. *Biophysical journal*, 84(4):2638–2645, 2003.
- [4] I. Khalil, H. Dijkslag, L. Abelman, and S. Misra. MagnetoSperm: A microrobot that navigates using weak magnetic fields. *Applied Physics Letters*, 104(22):223701, 2014.
- [5] Q. Fu, S. Guo, Y. Yamauchi, H. Hirata, and H. Ishihara. A novel hybrid microrobot using rotational magnetic field for medical applications. *Biomedical microdevices*, 17(2):1–12, 2015.
- [6] J. Mathieu and S. Martel. Aggregation of magnetic microparticles in the context of targeted therapies actuated by a magnetic resonance imaging system. *Journal of applied physics*, 106(4):044904, 2009.
- [7] S. Shaw and P. Murthy. Magnetic Drug Targeting in the Permeable Blood Vessel—The Effect of Blood Rheology. *Journal of Nanotechnology in Engineering and Medicine*, 1(2), 2010.



- [8] R. Tao and K. Huang. Reducing blood viscosity with magnetic fields. *Physical Review E*, 84(1):011905, 2011.
- [9] R. H. Ewoldt, M. T. Johnston, and L. M. Caretta. Experimental challenges of shear rheology: how to avoid bad data. In *Complex fluids in biological systems*, pages 207–241. Springer, 2015.
- [10] R. M. Turian. Perturbation Solution of the Steady Newtonian Flow in the Cone and Plate and Parallel Plate Systems. *Industrial & Engineering Chemistry Fundamentals*, 11(3):361–368, 1972.
- [11] R. Cardinaels, N. K. Reddy, and C. Clasen. Quantifying the errors due to overfilling for Newtonian fluids in rotational rheometry. *Rheologica Acta*, 58:525–538, 2019.
- [12] M. T. Johnston and R. H. Ewoldt. Precision rheometry: Surface tension effects on low-torque measurements in rotational rheometers. *Journal of Rheology*, 57(6):1515–1532, 2013.
- [13] G. A. Davies and J. R. Stokes. Thin film and high shear rheology of multiphase complex fluids. *Journal of Non-Newtonian Fluid Mechanics*, 148(1-3):73–87, 2008.
- [14] G. A. Davies and J. R. Stokes. On the gap error in parallel plate rheometry that arises from the presence of air when zeroing the gap. *Journal of Rheology*, 49(4):919–922, 2005.
- [15] J. Kramer, J. T. Uhl, and R. K. Prud’Homme. Measurement of the viscosity of guar gum solutions to  $50,000 \text{ s}^{-1}$  using a parallel plate rheometer. *Polymer Engineering & Science*, 27(8):598–602, 1987.
- [16] G. Vlemminckx and C. Clasen. On the Inseparability of Slip and Gap-Error. *Journal of Rheology*, 60(4):549–557, 2016.
- [17] J. Mewis and N. J. Wagner. *Colloidal suspension rheology*, volume 10. Cambridge University Press, 2012.
- [18] Richard Buscall. Wall slip in dispersion rheometry. *Journal of Rheology*, 54(6):1177–1183, 2010.
- [19] A. Yoshimura and R. K. Prud’homme. Wall slip corrections for Couette and parallel disk viscometers. *Journal of Rheology*, 32(1):53–67, 1988.
- [20] M. T. López-López, P. Kuzhir, S. Lacis, G. Bossis, F. González-Caballero, and J. D. G. Durán. Magnetorheology for suspensions of solid particles dispersed in ferrofluids. *Journal of Physics: Condensed Matter*, 18(38):S2803, 2006.
- [21] J. Laeuger, K. Wollny, H. Stettin, and S. Huck. A new device for the full rheological characterization of magneto-rheological fluids. *International Journal of Modern Physics B*, 19(07n09):1353–1359, 2005.

- [22] D. T. Grob, N. Wise, O. Oduwole, and S. Sheard. Magnetic susceptibility characterisation of superparamagnetic microspheres. *Journal of Magnetism and Magnetic Materials*, 452:134–140, 2018.
- [23] L. Campo-Deaño, R. Dullens, D. G. Aarts, F. T. Pinho, and M. S. N. Oliveira. Viscoelasticity of blood and viscoelastic blood analogues for use in polydimethylsiloxane in vitro models of the circulatory system. *Biomicrofluidics*, 7(3), 2013.
- [24] A. Volk and C. J. Kähler. Density model for aqueous glycerol solutions. *Experiments in Fluids*, 59(5):75, 2018.
- [25] M. M. Budeanu and V. Dumitrescu. Densities, viscosities and excess properties for dimethyl sulfoxide with diethylene glycol and Methyldiethanolamine at different temperatures. *Applied Sciences*, 12(1):116, 2021.
- [26] J. Soulages, M. S. N. Oliveira, P. C. Sousa, M. A. Alves, and G. H. McKinley. Investigating the stability of viscoelastic stagnation flows in T-shaped microchannels. *Journal of Non-Newtonian Fluid Mechanics*, 163(1-3):9–24, 2009.
- [27] M. S. N. Oliveira, R. Yeh, and G. H. McKinley. Iterated stretching, extensional rheology and formation of beads-on-a-string structures in polymer solutions. *Journal of non-Newtonian fluid mechanics*, 137(1-3):137–148, 2006.
- [28] L.E. Rodd, T. P. Scott, D. V. Boger, J. J. Cooper-White, and G. H. McKinley. The inertio-elastic planar entry flow of low-viscosity elastic fluids in micro-fabricated geometries. *Journal of Non-Newtonian Fluid Mechanics*, 129(1):1–22, 2005.
- [29] J. T. Ault, S. Shin, A. Garcia, A. Perazzo, and H. A. Stone. Viscosity measurements of glycerol in a parallel-plate rheometer exposed to atmosphere. *Journal of Fluid Mechanics*, 968:A2, 2023.
- [30] G. K. Batchelor. Sedimentation in a dilute dispersion of spheres. *Journal of fluid mechanics*, 52(2):245–268, 1972.
- [31] G. K. Batchelor. The effect of Brownian motion on the bulk stress in a suspension of spherical particles. *Journal of fluid mechanics*, 83(1):97–117, 1977.
- [32] J. de Vicente, M. T. López-López, J. D. G. Durán, and F. González-Caballero. Shear flow behavior of confined magnetorheological fluids at low magnetic field strengths. *Rheologica acta*, 44:94–103, 2004.
- [33] S. Melle, O. G. Calderón, M. A. Rubio, and G. G. Fuller. Microstructure evolution in magnetorheological suspensions governed by Mason number. *Physical Review E*, 68(4):041503, 2003.
- [34] Y. Gao, M. A. Hulsen, T. G. Kang, and J. M. J. Den Toonder. Numerical and experimental study of a rotating magnetic particle chain in a viscous fluid. *Physical Review E—Statistical, Nonlinear, and Soft Matter Physics*, 86(4):041503, 2012.

- [35] B. de Gans, H. Hoekstra, and J. Mellema. Non-linear magnetorheological behaviour of an inverse ferrofluid. *Faraday Discussions*, 112:209–224, 1999.
- [36] D. J. Klingenberg, J. C. Ulicny, and M. A. Golden. Mason numbers for magnetorheology. *Journal of Rheology*, 51(5):883–893, 2007.